2009

A regional scale modeling analysis of aerosol and trace gas distributions over the eastern Pacific during the INTEX-B field campaign

D. Adhikary

Brian G. Heikes
University of Rhode Island, bheikes@uri.edu

See next page for additional authors

Authors

D. Adhikary, Brian G. Heikes, and et al

Atmospheric
Chemistry
and Physics

A regional scale modeling analysis of aerosol and trace gas distributions over the eastern Pacific during the INTEX-B field campaign

B. Adhikary[1,2], G. R. Carmichael[1], S. Kulkarni[1], C. Wei[1], Y. Tang[1,*], A. D'Allura[1,**], M. Mena-Carrasco[1,***],
D. G. Streets[3], Q. Zhang[3], R. B. Pierce[4,****], J. A. Al-Saadi[4], L. K. Emmons[5], G. G. Pfister[5], M. A. Avery[4],
J. D. Barrick[4], D. R. Blake[6], W. H. Brune[7], R. C. Cohen[8], J. E. Dibb[9], A. Fried[5], B. G. Heikes[10], L. G. Huey[11],
D. W. O'Sullivan[12], G. W. Sachse[4], R. E. Shetter[5], H. B. Singh[13], T. L. Campos[5], C. A. Cantrell[5], F. M. Flocke[5],
E. J. Dunlea[14,*****], J. L. Jimenez[14], A. J. Weinheimer[5], J. D. Crounse[15], P. O. Wennberg[15], J. J. Schauer[16],
E. A. Stone[16], D. A. Jaffe[17], and D. R. Reidmiller[18]

[1]Center for Global and Regional Environmental Research, University of Iowa, Iowa City, IA 52242, USA
[2]School of Engineering, Kathmandu University, Dhulikhel, Kavre, Nepal
[3]Decision and Information Sciences Division, Argonne National Laboratory, Argonne, IL, USA
[4]NASA Langley Research Center, Hampton, VA, USA
[5]National Center for Atmospheric Research, Boulder, CO, USA
[6]Department of Chemistry, University of California, Irvine, CA, USA
[7]Department of Meteorology, Penn State University, University Park, PA, USA
[8]Department of Chemistry, University of California, Berkeley, CA, USA
[9]Institute for the Study of Earth, Oceans and Space, University of New Hampshire, Durham, NH, USA
[10]Graduate School of Oceanography, University of Rhode Island, Narragansett, RI, USA
[11]School of Earth and Atmospheric Sciences, Georgia Institute of Technology, Atlanta, GA, USA
[12]United States Naval Academy, Annapolis, MD, USA
[13]NASA Ames Research Center, Moffett Field, CA, USA
[14]Department of Chemistry and Biochemistry, and CIRES, University of Colorado, Boulder, CO, USA
[15]California Institute of Technology, Pasadena, CA, USA
[16]Environmental Chemistry and Technology, College of Engineering, University of Wisconsin-Madison, Madison, WI, USA
[17]University of Washington, Bothell, WA 98011, USA
[18]Department of Atmospheric Sciences/University of Washington, Seattle, WA 98195, USA
*now at: NOAA/NCEP/EMC, Camp Springs, MD, USA
**now at: ARIANET Srl, Milano, Italy
***now at: Universidad Andrés Bello, Santiago, Chile
****now at: NOAA/NESDIS, Madison, WI, USA
*****now at: NOAA Climate Program Office, Silver Spring, MD, USA

Abstract. The Sulfur Transport and dEposition Model (STEM) is applied to the analysis of observations obtained during the Intercontinental Chemical Transport Experiment-Phase B (INTEX-B), conducted over the eastern Pacific Ocean during spring 2006. Predicted trace gas and aerosol distributions over the Pacific are presented and discussed in terms of transport and source region contributions. Trace species distributions show a strong west (high) to east (low) gradient, with the bulk of the pollutant transport over the central Pacific occurring between ~20° N and 50° N in the

Correspondence to: S. Kulkarni
(sarika-kulkarni@uiowa.edu)

2–6 km altitude range. These distributions are evaluated in the eastern Pacific by comparison with the NASA DC-8 and NSF/NCAR C-130 airborne measurements along with observations from the Mt. Bachelor (MBO) surface site. Thirty different meteorological, trace gas and aerosol parameters are compared. In general the meteorological fields are better predicted than gas phase species, which in turn are better predicted than aerosol quantities. PAN is found to be significantly overpredicted over the eastern Pacific, which is attributed to uncertainties in the chemical reaction mechanisms used in current atmospheric chemistry models in general and to the specifically high PAN production in the SAPRC-99 mechanism used in the regional model. A systematic underprediction of the elevated sulfate layer in the eastern Pacific observed by the C-130 is another issue that is identified and discussed. Results from source region tagged CO simulations are used to estimate how the different source regions around the Pacific contribute to the trace gas species distributions. During this period the largest contributions were from China and from fires in South/Southeast and North Asia. For the C-130 flights, which operated off the coast of the Northwest US, the regional CO contributions range as follows: China (35%), South/Southeast Asia fires (35%), North America anthropogenic (20%), and North Asia fires (10%). The transport of pollution into the western US is studied at MBO and a variety of events with elevated Asian dust, and periods with contributions from China and fires from both Asia and North America are discussed. The role of heterogeneous chemistry on the composition over the eastern Pacific is also studied. The impacts of heterogeneous reactions at specific times can be significant, increasing sulfate and nitrate aerosol production and reducing gas phase nitric acid levels appreciably (∼50%).

1 Introduction

Economic development in the last few decades throughout much of Asia has led to rapid increase in anthropogenic emissions of aerosols and trace gases (Streets et al., 2003; Garg et al., 2006; Zhang et al., 2009). Studies have shown that some of these aerosols and trace gases emitted from Asia reach North America and significantly enhance ozone and aerosol concentration over background levels (Jaffe et al., 1999; VanCuren 2003; Hadley et al., 2007; Van Donkelaar et al., 2008; Zhang et al., 2008). The transport of pollutants from the Asian mid-latitudes to North America is particularly strong during the spring season (Yienger et al., 2000; Bey et al., 2001; Liang et al., 2004). Long range transport of aerosols and gaseous pollutants could partially offset domestic emission controls over North America (Liu et al., 2008). In addition, rising Asian aerosol emissions may have a climatic impact on North America (Levy et al., 2008).

In the recent decade several airborne field campaigns have been conducted to study the rising impact of Asian pollution over the Pacific and North America. The TRACE-P (Jacob et al., 2003) and ACE-Asia (Seinfeld et al., 2004) field campaigns studied the outflow of Asian emissions to the western Pacific during the spring of 2001. PHOBEA-II and ITCT-2K2 field campaigns were undertaken to characterize the atmospheric environment of the eastern Pacific during the spring of 2002 (Bertschi et al., 2004). The Intercontinental Chemical Transport Experiment, Phase B (INTEX-B) campaign was conducted during the spring of 2006 by the National Aeronautics and Space Administration (NASA) (Singh et al., 2009).

One of the scientific objectives of the INTEX-B field campaign was to understand the transport and evolution of Asian pollution with implications for North American air quality and climate. Multiple airborne measurements from the NASA DC-8 and the NSF/NCAR C-130 aircraft were made to characterize the atmospheric environment of the Pacific and western North America (Dunlea et al., 2009; McNaughton et al., 2009; Shinozuka et al., 2009; Singh et al., 2009). The INTEX-B campaign, with the NASA DC-8 aircraft stationed over Hawaii and Anchorage and the NSF/NCAR C-130 stationed over Seattle, provided a much better geographical coverage of the inflow of Asian emissions to the east central Pacific and western North America. In addition to the airborne measurements, observations from different remote sensing instruments on board the NASA satellites and various ground based surface stations were also made (e.g. Wolfe et al., 2007; Reidmiller et al., 2009).

Global and regional chemical transport models were used to assist the flight planning of the airborne observation missions during INTEX-B. Chemical transport models (CTMs) provide valuable means to link observed pollutant concentrations with their emission sources. The Sulfur Transport and dEposition Model (STEM), a regional chemical transport model, has been previously used to assist in flight planning activities and to interpret the measurements from multiple platforms in several other field campaigns including the ACE-Asia (Tang et al., 2004b), TRACE-P (Carmichael et al., 2003), ITCT-2k2 (Tang et al., 2004a) and ICARTT (Mena-Carrasco et al., 2007; Tang et al., 2007).

During the INTEX-B field campaign, STEM was used in the flight planning and to interpret observations made from the airborne platforms. This is the first application of the regional scale STEM model to such a large geographic area that covers the source regions of Asia, the Pacific and western North America as seen in Fig. 1. This spatial coverage is generally obtained through global scale models at a coarser horizontal resolution. The large spatial extent of the STEM model domain has provided a great opportunity to study the inflow of Asian aerosols into the Pacific and North America (NA).

In this study we use our regional scale model to investigate the distributions of trace gases and aerosols over the

Pacific and to estimate how anthropogenic, biomass burning and wind blown dust emissions from various geographical regions impact these distributions. We know from previous studies that the outflow from these sources into the Pacific is characterized by high aerosol loadings. Tang et al. (2003) evaluated the role of aerosols in influencing photochemistry over the western Pacific during the TRACE-P mission. The study found that aerosol influence via photolysis rate (J-values) reduced OH by 40% below 1 km and by 24% above 1 km. The INTEX-B airborne observations constrain the model across a wider geographical region and provide an opportunity to examine the contribution of aerosols in influencing photochemistry farther away from the source region.

Aerosols can also influence atmospheric chemistry by providing surface area where reactions can occur (Grassian, 2002). A previous version of STEM has been used to study the impact of heterogeneous chemistry on dust surfaces during the ACE-Asia campaign (Tang et al., 2004b). The results from ACE-Asia study showed that near the surface layer heterogeneous reactions decreased the concentration of O_3, SO_2, NO_2 and HNO_3 by 20%, 55%, 20% and 95%. The INTEX-B observations again allow us to study the influence of heterogeneous reactions with a longer time for aerosol transport, mixing and aging.

We also use the model to investigate the relative contributions of distant sources of pollutants relative to more local sources on the observations at the Mt. Bachelor Observatory (MBO, 44.0° N, 121.7° W, 2.7 km altitude above sea level (a.s.l.) in Oregon), which obtained measurements in conjunction with the airborne observations during INTEX-B. This is a topic of growing interest due to the changing emission patterns along the Pacific Rim.

The paper is structured as follows. We first present a description of our regional model and the emissions inventory used in this study (Sect. 2). The regional aerosol and trace gas distributions are described in Sect. 3.1. The mission-mean spatial distributions of trace gases and aerosols and the contributions from regional anthropogenic and biomass burning emissions are presented in Sect. 3.2. The results of the model intercomparison with DC-8 and C-130 aircraft observations are presented in detail (Sect. 3.3). The transport of trace gases and aerosols across the Pacific and the impact of this transport on the western USA are discussed in Sect. 3.4. Finally, we present the impact of heterogeneous chemistry on dust aerosol surfaces and the contribution of aerosols in influencing photochemistry over the Pacific (Sect. 3.5) followed by conclusions (Sect. 4).

2 Model description and emissions inventory

STEM was developed at the University of Iowa in the early 1980s (Carmichael et al., 1986) and has continuously undergone development since then to its current version which is
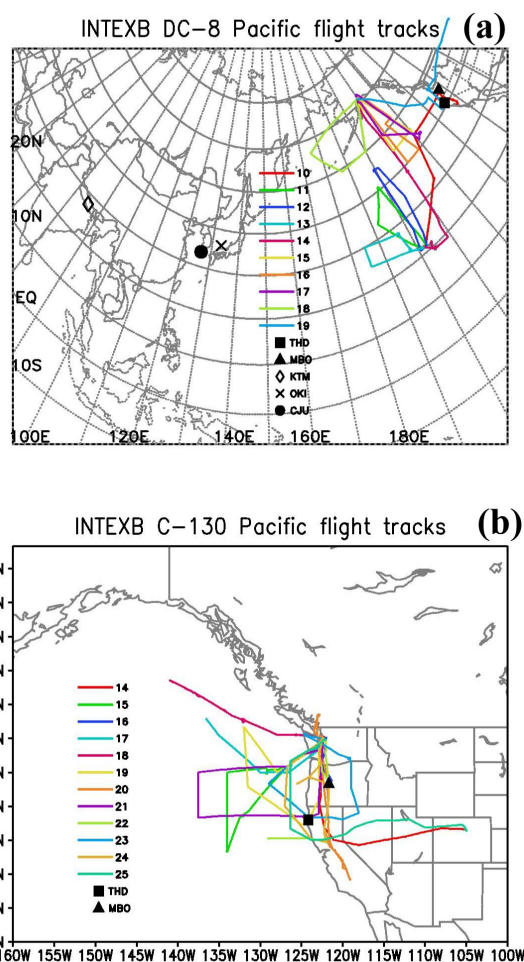

Fig. 1. NASA DC-8 and NCAR/NSF C-130 flight tracks along with the location of ground based observation sites including Kathmandu (KTM) Nepal, Oki (OKI) Japan, Cheju (CJU) South Korea, Trinidad Head (THD), Mt. Bachelor (MBO) during the INTEX-B (Phase 2) experiment. The numbers denote the Research Flight (RF) numbers for the DC-8 and C-130 aircraft.

the STEM-2K3 version (Tang et al., 2007). STEM is a regional chemical transport model which features the SAPRC-99 chemical mechanism (Carter, 2000). Online photolysis rate calculations in the STEM are performed using the TUV (Tropospheric Ultra-Violet Radiation) model (Madronich, 2002). The TUV model needs total ozone column to calculate the absorption of UV radiation by ozone molecules. For this study, we used the daily column ozone data from the Ozone Mapping Spectrometer (OMI) instrument on board the NASA Aura spacecraft. Thirty different photolysis rates are calculated using the STEM-TUV model. The STEM uses the SCAPE II (Simulating Composition of Atmospheric Particles in Equilibrium Aerosol Solver) aerosol module to simulate inorganic gas to particle conversion and aerosol particle growth (Kim et al., 1995). The inorganic aerosols in the STEM-SCAPE model are binned into four size bins of 0.1–

0.3 μm, 0.3–1.0 μm, 1.0–2.5 μm and 2.5–10.0 μm. The model was run for the entire INTEX-B field campaign with 1 week for model spin up.

STEM does not require a uniform horizontal grid and can be mapped to any map projection based on the meteorological model. The STEM preprocessor extracts all of the topography and other land use variables that were used in the meteorological model along with the meteorological parameters necessary for simulating chemical transport and removal processes. Thus, STEM has the same map projection and grid resolution as the meteorological model. For this study, we used the WRF-ARW (Weather Research Forecasting) Version 2.1.2 meteorological model developed at NCAR (Skamarock et al., 2005). The WRF model horizontal resolution was 50×50 km with 314×200 grid cells, and 21 vertical levels with the model top at 50 hPa. The vertical spacing in the WRF model was defined to have the highest density in the first km. The chemistry model was simulated with the first 18 layers reaching up to 10.5 km above ground layer (a.g.l.) height. Significant stratospheric air-mass intrusion within the model domain at higher latitudes (without any stratospheric chemistry/parameterization in STEM) limited the chemistry model's ability to simulate higher altitudes. GFS $1° \times 1°$ model forecast at 18:00 UTC from the National Center for Environmental Prediction (NCEP) was used for initialization and boundary conditions at a 6 h interval in the WRF calculations. The physics options used in the WRF model are as follows: WSM-3 class simple ice scheme for microphysics; RRTM scheme for longwave/shortwave radiation; Monin-Obukhov scheme for surface layer; Noah land-surface model; YSU scheme for the boundary layer; and the Grell-Devenyi ensemble scheme for the cumulus parameterization. Evaluation of WRF model prediction skills with INTEX-B observation is presented in a later section (Sect. 3.3).

Gridded anthropogenic emissions for Asia were obtained from the emissions inventory developed for the INTEX-B mission described in detail by Zhang et al. (2009). The horizontal resolution of the gridded emissions inventory was $0.5° \times 0.5°$ extending from 8° N–50° N and from 80° E–150° E. Emissions of volatile organic compounds were available based on the SAPRC-99 speciation. The National Emissions Estimate (NEI-2001v3) was used as emissions for the North American region. This emissions inventory has been previously used to study the regional air quality over North America during the ICARTT mission (Mena-Carrasco et al., 2007; Tang et al., 2007). For regions outside the Asia and North America the global emissions inventory from the EDGAR database (Olivier et al., 2001) was used. Daily emissions forecast from biomass burning were available from the Regional Air Quality Modeling System (RAQMS) modeling group during the INTEX-B field campaign (Al-Saadi et al., 2008). We used the same biomass burning emissions for this post field mission study. Biogenic emissions of terpene and isoprene were taken from a 12 year averaged data obtained from the ORCHIDEE model (Lathiere et al., 2006). It has been shown that using the top and lateral boundary conditions from a global model enhances the STEM prediction skill (Tang et al., 2007). We used the Model for Ozone and Related Chemical Tracers (MOZART-4) global model to provide top and lateral boundary conditions (Pfister et al., 2008) for this study. Dust emissions were calculated online using a parameterization based on previous studies using STEM (Tang et al., 2004b; Uno et al., 2004). Emissions of sea salt within STEM were based on the work by S. L. Gong (Gong, 2003).

3 Results and discussion

3.1 Spatial distribution of trace gases and aerosols

Figure 1a shows the horizontal modeling domain of the WRF-STEM model used in this study. Figure 1a and b also show the flight tracks of the DC-8 and the C-130 during the INTEX-B field campaign. The DC-8 flights span the region of the central Pacific from southern Alaska to Hawaii, while the C-130 airborne observations cover a large portion of the eastern Pacific off the coast of the Northwest USA. Figure 1 also shows the location of ground based measurement stations including Mt. Bachelor (MBO) Oregon, Trinidad Head (THD) California, Cheju (CJU) South Korea, Oki (OKI) Japan and Kathmandu (KTM) Nepal discussed later in this paper.

The modeled mission-mean distributions of CO, O_3 and PAN at 3 km a.g.l. for the INTEX-B period (15 April–15 May 2006) are shown in Fig. 2, and provide a context for the conditions under which the aircraft experiments were conducted. The CO distribution (Fig. 2a) reveals emission hotspots associated with anthropogenic sources (such as those over India and eastern China), and those associated with open biomass burning (e.g., northern Thailand and Vietnam and western Russia). These sources are larger than the North American anthropogenic and open burning emissions for this domain and time period, resulting in a significant west to east gradient of decreasing CO. The CO distribution also shows the influence of intercontinental transport of CO into the domain above 30° N through the boundary conditions provided by the global model MOZART. Due to these major CO inputs and the transport patterns over the Pacific during this period, the region of enhanced CO (>120 ppb) shifts northward during transport over the Pacific, with peak values at latitudes greater than 30° N over the eastern Pacific. The source contributions and vertical structure will be discussed in more detail in Sect. 3.2.

The mission-mean ozone distribution at 3 km a.g.l. (Fig. 2c) shows strong enhancements (>70 ppb) between ~25° N and 35° N over the Asian continent, due to a combination of stratospheric influence (e.g., over the Tibetan Plateau) and anthropogenic activities (e.g., eastern China and

Japan). The influence of anthropogenic emissions from and around major cities (e.g., Delhi, Kolkata, Los Angeles) and around the major open biomass burning areas in Siberia and Alaska are also identified. The ozone distribution shows a stronger zonal pattern than CO, with a much smaller contribution from the high latitude boundaries. The mission-mean PAN distribution (Fig. 2e) shows a region of high photochemical production over East Asia, which can help separate the regions of stratospheric influence from anthropogenic influence of the ozone distribution discussed above. The long range transport of PAN at high latitudes into the region is clearly shown and reflects the lower temperature of the inflow air during the mission period.

The mission-mean horizontal distributions of aerosol sulfate, nitrate and dust are also presented in Fig. 2b, d, and f, respectively. These aerosol distributions show a stronger zonal pattern than the gas species discussed previously, reflecting the fact that the aerosols typically have a shorter lifetime and thus are less influenced by continental transport and more dominated by emission source regions. For example, sulfate shows a strong west to east gradient, with the peak values in the west reflecting the heavy populated and industrial regions of India and China, and is transported across the Pacific at latitudes between $20°$ N–$30°$ N. Particulate nitrate has a different pattern, with elevated levels on both sides of the Pacific reflecting regions with high NO_x and NH_3 emissions. The relative importance of sulfate with respect to nitrate decreases from west to east across the Pacific, with nitrate dominating over California. Both sulfate and nitrate show enhancements due to Hawaii emissions from anthropogenic and volcanic sources (in the case of sulfate). The dust distribution shows maximum values in the western part of the domain reflecting the strong source regions during this time period (i.e., Central Asia and China), and the region of elevated levels of dust extend across the Pacific, which impacts the chemistry as discussed later in Sect. 3.5.

3.2 Source/region contributions

To more clearly identify the contributions from anthropogenic and open burning sources to the distribution of trace species over the Pacific, additional model calculations were performed using CO tracers from tagged source regions. For these calculations the anthropogenic and biomass components of the CO emission inventory were broken into regions. The global model MOZART also used CO tracers from tagged source regions and these were used as boundary conditions for the tagged runs. In this way the impact of NA CO transported around the globe and back into the Pacific via the western and northern boundaries could be estimated. The mission-mean contribution from various sources and regions at 3 km a.g.l. are shown in Fig. 3. The results are expressed in terms of % contribution from a particular source/region to the total primary CO distribution calculated using all sources. Biomass burning emissions (Fig. 3b) contribute significantly

($>20\%$) throughout the Pacific basin, with Siberia fire emissions (Fig. 3d) being transported across the Pacific at latitudes above $\sim 35°$ N, and emissions from South/Southeast Asia (Fig. 3f) fires transported predominantly at latitudes below $\sim 35°$ N. Anthropogenic emissions from China (Fig. 3c) is the largest single contributor to CO over large parts of the Pacific for this time period. Anthropogenic emissions from South/Southeast Asia (Fig. 3e) are smaller than the emissions from biomass burning emissions (Fig. 3f) in these regions. In the eastern Pacific anthropogenic emissions from North America have the largest impact on the CO distribution.

Further insights into the distribution of CO and the contributions of various source regions to the CO distributions over the Pacific are shown in the cross section plots in Fig. 4. In Fig. 4a the CO distribution from the full chemistry simulation along $45°$ N shows strong zonal transport with CO transported into the domain from Europe largely within the boundary layer as seen in the distribution in the western portion of the domain (i.e., $<100°$ E longitude). The CO emissions from East Asia are transported out over the Pacific via frontal systems resulting in lifting of the CO above the boundary layer and into the free troposphere. The bulk of the transported CO is at altitudes of 3–5 km as shown in the zonal cross section along $145°$ E longitude (Fig. 4c). As the polluted air-masses reach the eastern Pacific, the frontal systems tend to move poleward, and aged air-masses subside and mix with CO emitted from North America leading to enhanced CO levels within the boundary layer as shown in the $125°$ W zonal cross section (Fig. 4g).

Also shown in Fig. 4 are the cross sections for the China CO tracer. The meridional cross section along $45°$ N (Fig. 4b) shows the major outflow of China CO at an altitude of ~ 3 km. The lifetime of CO is such (about 1–2 months, Liang et al., 2004) that it can be transported globally as shown by the inflow of aged China CO air-masses coming into the region at the western boundary of the domain at altitudes above 5 km via the boundary conditions provided by the global MOZART model (which also included source region tagged CO tracers). Comparison of Fig. 4a and b at the western boundary shows that intercontinental transport of CO from Europe occurs largely within the boundary layer, while transport from Asia and North America (not shown) re-enter the domain largely at higher altitudes. The China CO distributions at $160°$ W (Fig. 4f) and $125°$ W (Fig. 4h) (the regions where the DC-8 and C-130 operated, respectively) show the maximum China influence between $\sim 30°$ N and $60°$ N and from 3 km to 9 km, with values exceeding 20 ppb. The $160°$ W (Fig. 4f) plot shows that while the major transport patterns move China emissions to areas above $30°$ N, there are transport pathways that move China emissions to lower latitudes (see the feature near the equator). During individual transport events a portion of the China emissions get caught in subsiding motions and transported to lower latitudes, and subsequently transported in the low altitude easterlies.
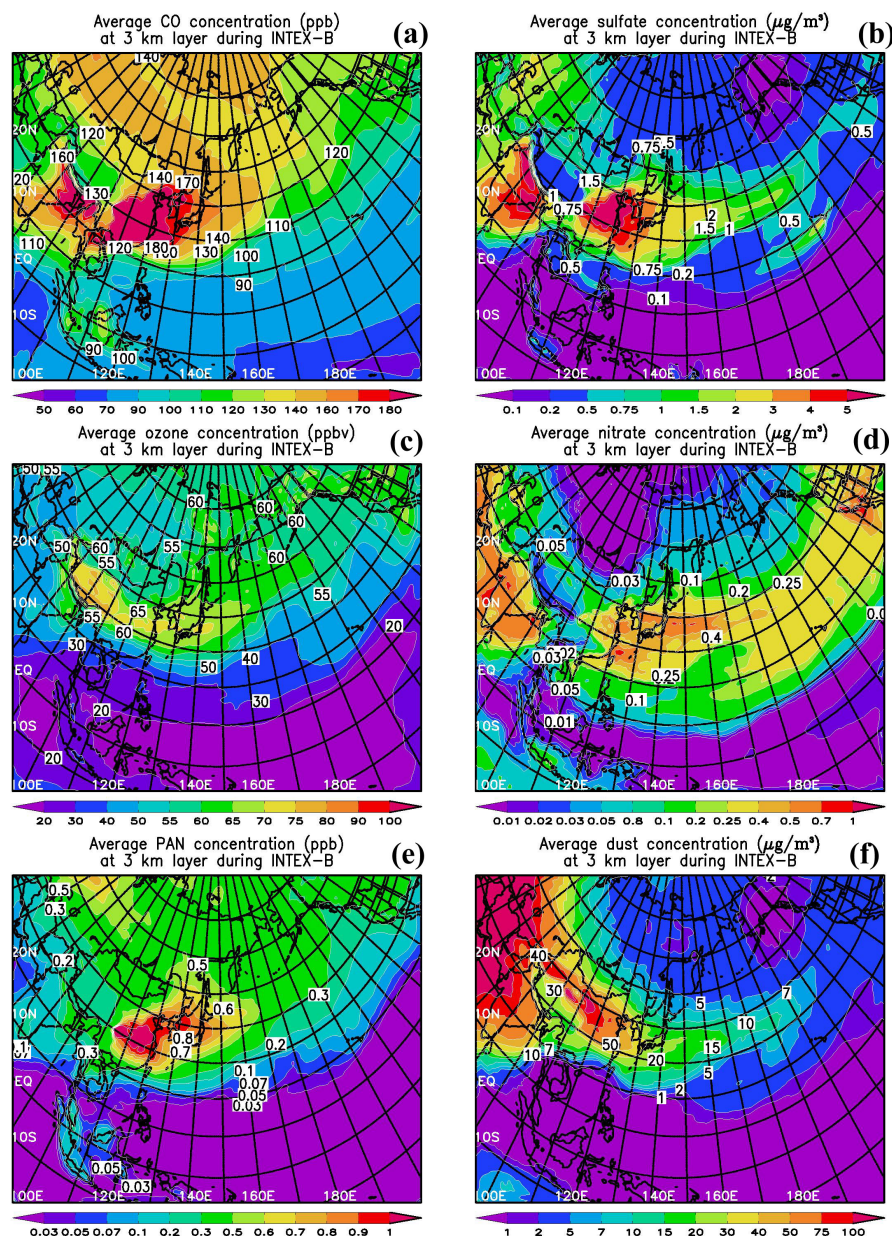
Fig. 2. Mission-wide average distributions of trace gases and aerosols at 3 km a.g.l. during INTEX-B **(a)** CO (ppb) **(b)** Sulfate (μg/m^3) **(c)** Ozone (ppb) **(d)** Nitrate (μg/m^3) **(e)** PAN (ppb) and **(f)** Dust (μg/m^3). The values on the maps denote the contour labels at sharp gradients.

The results for 125° W (Fig. 4h) can be compared to the transpacific transport of CO analyzed by Forster et al. (2004) in support of the ITCT-2k2 experiment conducted in April–May 2004 in the eastern Pacific (Forster et al, 2004). They analyzed Asian transport using Asia tagged CO in the FLEX-PART model. Our results (Fig. 4h) share several similarities with theirs (see Forster et al., 2004 Fig. 4). Both sets of results show the Asian contribution beginning at ∼20° N and extending throughout the depth of the troposphere, with the maximum contributions at latitudes greater than 30° N and

at altitudes ∼8 km. Our mean values of the China CO contribution are significantly higher than Forster et al. (2004) (∼25 vs. 5 ppb) which is expected as their results only included contributions from air-masses younger than 20 days and were based on emissions representative of 1990.

3.3 Comparison with aircraft observations

In previous studies, we evaluated the model's capability in simulating Asian outflow into the western Pacific (cf.,
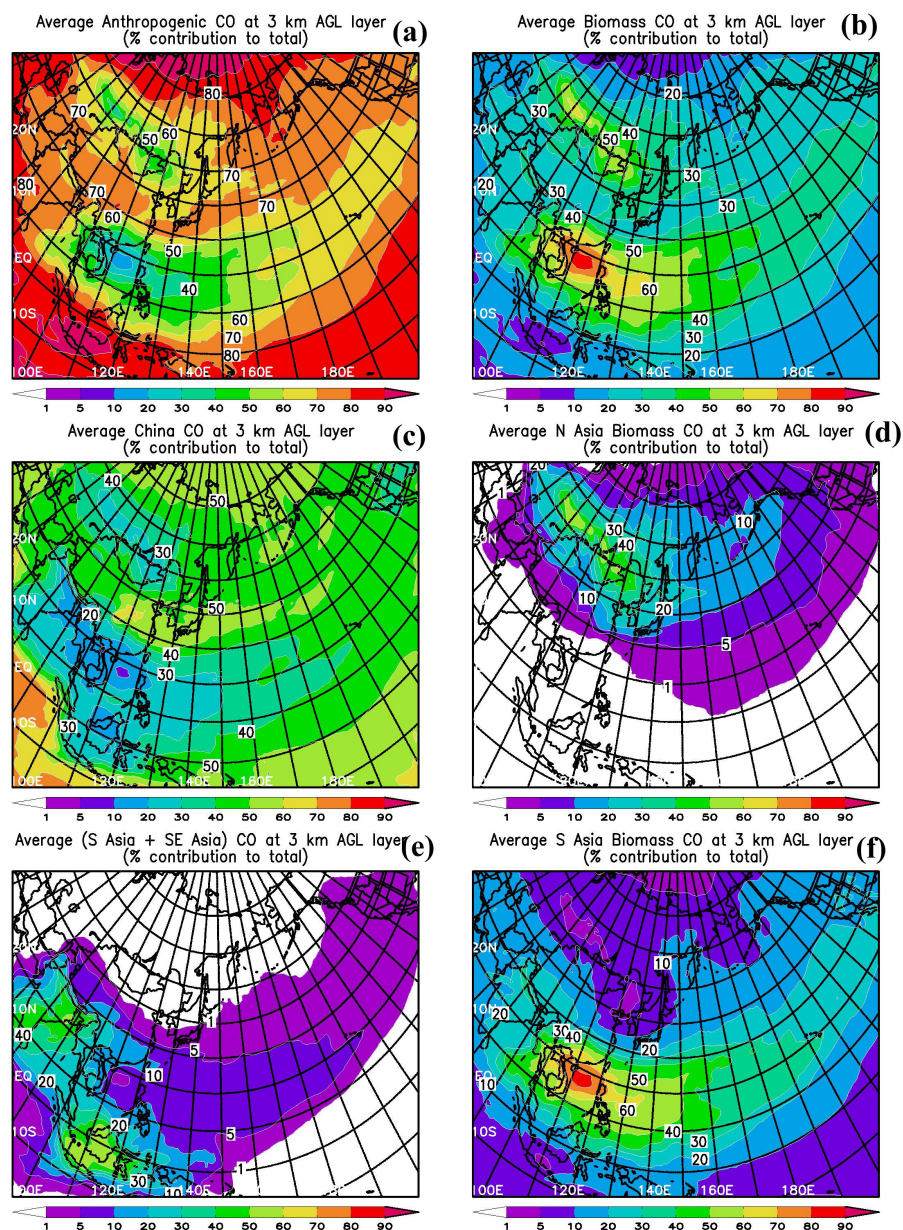
Fig. 3. Mission-wide average percent (%) contributions from source regions to total primary CO (anthropogenic + biomass) at 3 km a.g.l. during INTEX-B **(a)** Anthropogenic CO **(b)** Biomass CO **(c)** China CO **(d)** North Asia (>40° N) biomass CO **(e)** South/Southeast Asia anthropogenic CO **(f)** South/Southeast Asia biomass CO. The values on the maps denote the contour labels at sharp gradients.

Carmichael et al., 2003). This is the first time that we have applied STEM over a domain this large, and thus this presents an opportunity to evaluate the model for the eastern Pacific under conditions of very long range transport (∼10 days). A mission-wide summary of the model predictions compared to the observations is presented in Tables S1 and S2 of the supplemental materials (see http://www.atmos-chem-phys.net/10/2091/2010/acp-10-2091-2010-supplement.pdf). Observed and modeled species mean values, standard deviation, and correlation coefficient, R, are presented for various altitudes. In Fig. 5, we show the ratio of observed to predicted mean values for 30 different parameters at various altitudes. For most parameters the predicted values are within a factor of 2 (or smaller) of the observations. The largest differences occur for nitric acid (significantly underpredicted) and particulate nitrate (overpredicted), and we believe this is related to the calculation of partitioning between gas and aerosol phases
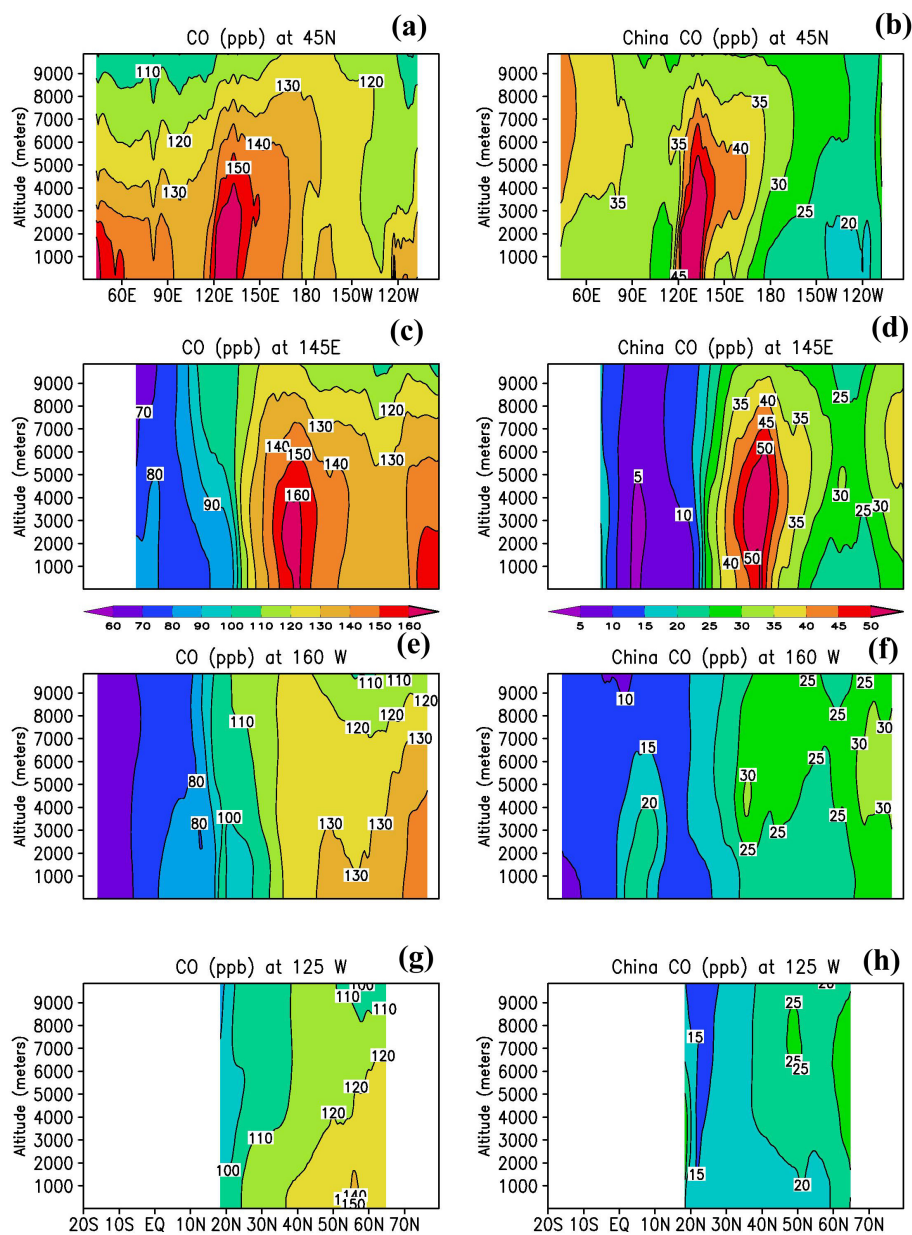
Fig. 4. Mission-wide average latitudinal and longitudinal distributions during INTEX-B **(a)** Meridional cross section of CO at 45° N **(b)** Meridional cross section of China CO at 45° N **(c)** Zonal cross section of CO at 145° E **(d)** Zonal cross section of China CO at 145° E **(e)** Zonal cross section of CO at 160° W **(f)** Zonal cross section of China CO at 160° W **(g)** Zonal cross section of CO at 125° W **(h)** Zonal cross section of China CO at 125° W. The values on the cross section plots denote the contour labels at sharp gradients.

as discussed later in the paper (Sect. 3.3.2). In a previous study during the TRACE-P mission we found that STEM reproduced observations better at lower altitudes (Carmichael et al., 2003). For INTEX-B, we do not see as strong of an altitude dependency in the model prediction skill. The results show that meteorological variables are generally better predicted than gas phase species, which in turn are better predicted than aerosol quantities. Further details are presented in the supplemental materials. Below we discuss in more detail a subset of the evaluated parameters.

3.3.1 Meteorological parameters

This was the first time that we applied the WRF model to drive our chemical transport model. The WRF model skill was evaluated for four key meteorological parameters (i.e. temperature, Relative Humidity (RH), wind speed and wind direction) essential for chemical transport with observations onboard the DC-8 and C-130 in Fig. 6. The predicted and observed DC-8 and C-130 values for all flights, shown in Fig. 6, are stratified and averaged into 1000 and 500 m bins
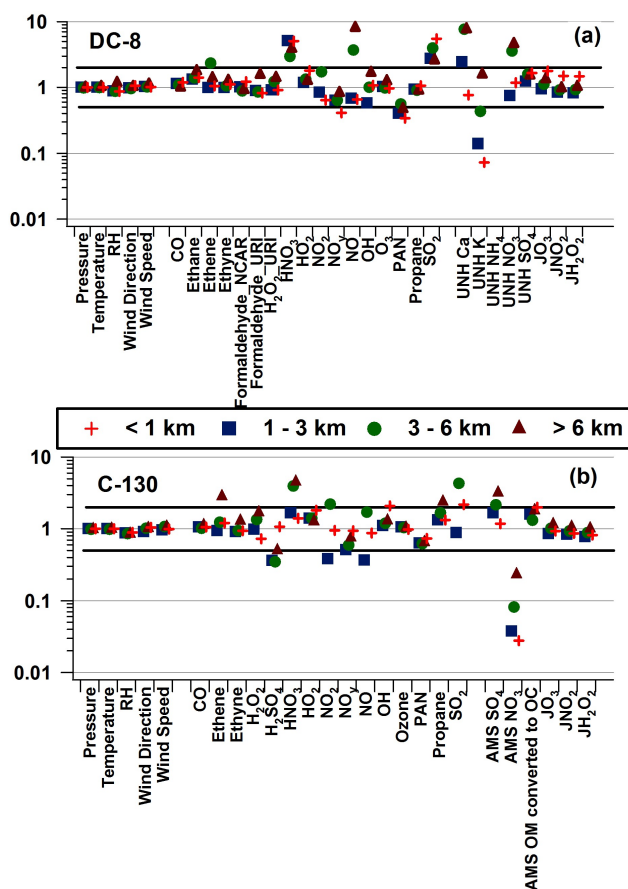
Fig. 5. Ratio of observed to model predicted mission-mean values at various altitudes for airborne measurements during INTEX-B **(a)** DC-8 and **(b)** C-130.

Fig. 6. Comparison of meteorological variables from the WRF model with DC-8 (top row) and C-130 (bottom row) observations **(a)** DC-8 temperature (°K) **(b)** DC-8 Relative Humidity (%) **(c)** DC-8 wind speed (m/s) **(d)** DC-8 wind direction (deg) **(e)** C-130 temperature (°K) **(f)** C-130 Relative Humidity (%) **(g)** C-130 wind speed (m/s) **(h)** C-130 wind direction (deg).

respectively based on flight altitude. The horizontal error bars in Fig. 6 represent the standard deviations of the observed and simulated values. In general the model does a good job in representing the meteorology during this period. Notable differences are seen in RH (Fig. 6b and f) where the model has a small positive bias in the lower troposphere, a larger negative bias in the upper troposphere, and is not able to capture the high variability seen in the observations at higher altitudes. The predicted horizontal winds (Fig. 6c and g) show a small negative bias in speed, that is most apparent at altitudes around 10 km, while the direction for the C-130 (Fig. 6h) is biased high below 3 km, and biased low at higher altitudes. For both wind speed and direction the predicted fields show similar variability as the observations.

3.3.2 Trace gases

The CO predictions are compared with DC-8 and C-130 observations in Fig. 7a and d, respectively. The model under-predicts CO at altitudes below ∼5 km, to a greater extent for the DC-8 (∼20 ppb, 15%) than for the C-130 flights (∼7 ppb;
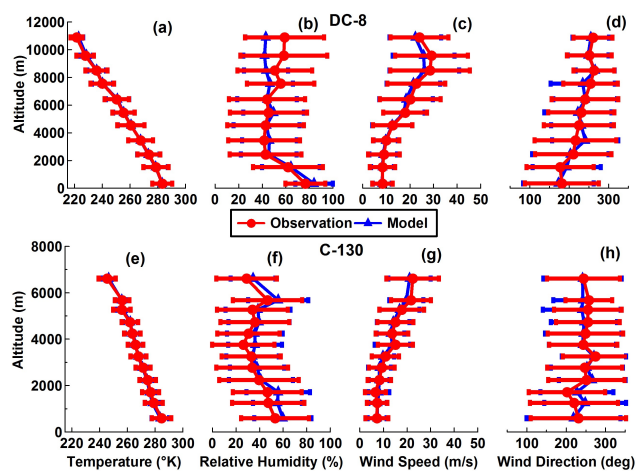
6%). Similar results were found in global model simulations for INTEX-B (Zhang et al., 2008). The underprediction of CO over the central Pacific below 3 km is larger than indicated by the absolute error. The net CO enhancement observed in this region is ∼40 ppb (assuming a background level of 100 ppb), which the model underestimates by a factor of 2. At higher altitudes, the model shows a slight positive bias with respect to the DC-8 observations. We investigated the contribution of emissions from North America (NA) to the C-130 vertical distributions by comparing the vertical CO distributions only for flight segments west of 125° W in Fig. 7d. The contribution from NA sources is ∼10 ppb extending to ∼4 km. We also see that the distribution become flatter and more similar to the DC-8 distributions when the NA influence is removed.

The underprediction of CO suggests that the Asian emissions are underestimated. Both the biomass burning and anthropogenic emissions contribute significantly to the CO distributions in the areas sampled by the DC-8/C-130 aircraft and these emissions are highly uncertain. The underestimation in predicted CO is well within the uncertainty of the estimates of anthropogenic and open biomass CO emissions (>150%, Streets et al., 2003). Furthermore the DC-8 flights sampled along 160° W, which had a strong gradient in CO as discussed earlier in the cross section plot of CO at 160° W (Fig. 4e). Here the predicted mean profiles of CO show low altitude enhancements (with CO between 130–140 ppb) at latitudes greater than ∼45° N, while those at lower latitudes do not. The underprediction in the boundary layer enhancement in CO for the DC-8 flights could also be due in part to a slight spatial displacement in the predicted distributions
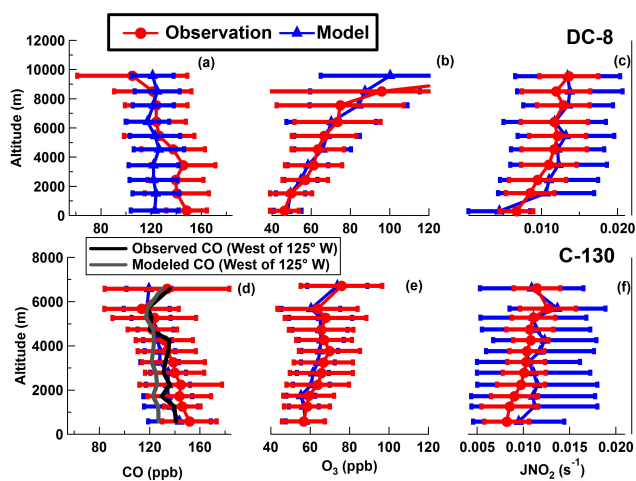
Fig. 7. Comparison of STEM model predictions with DC-8 (top row) and C-130 (bottom row) observations of **(a)** DC-8 CO (ppb) **(b)** DC-8 Ozone (ppb) **(c)** DC-8 photolysis rate of NO$_2$ (JNO$_2$) (s^{-1}) **(d)** C-130 CO (ppb) **(e)** C-130 Ozone (ppb) **(f)** C-130 photolysis rate of NO$_2$ (JNO$_2$) (s^{-1}).

as described above. While such a displacement is not apparent from the meteorological comparison, small errors after 10-day transport could become a factor.

For ozone (Fig. 7b and e), the model accurately captures the main features in the observed ozone vertical distributions for both the DC-8 and C-130. The C-130 predictions (Fig. 7e) have a small negative bias (~3 ppb) in the midtroposphere. Both the observations and the model show lower variability for the DC-8 flight locations than for the C-130 flights (for which the model underestimates the variability). These vertical distributions along with the horizontal distribution in Fig. 2c show that ozone over the eastern Pacific is significantly enhanced above the boundary layer. The impact of this feature on ozone concentration in the western US is discussed further in Sect. 3.4.3.

An evaluation of the STEM-TUV model prediction of the photolysis rates (J-value) for NO$_2$, a critical step in the formation of ozone, is shown in Fig. 7c and f. The calculation of J-NO$_2$ depends on the overhead column of ozone and the vertical distributions of ambient aerosol and clouds. Thus it is a good test of multiple parameter predictions. In general the model is able to capture the magnitude of observed J-NO$_2$ and the general features in the vertical structure. However, modeled J-NO$_2$ shows a general overprediction compared to observations, and a significantly higher variability than observed. The high variability in the calculated J-values will be discussed further in Sect. 3.5.

To further test the consistency between the modeled and observed photochemical oxidant cycles, we next compare nitrogen oxide distributions. Figure 8 presents the gas phase NO, NO$_2$ PAN and HNO$_3$ model vs. aircraft comparisons. The predicted values of the sum of these four species cap-

ture many of the important features of the DC-8 and C-130 observations, including the shape of the vertical distributions and the strong enhancement in the C-130 values below 3 km. However the model overpredicts the sum by ~20%. In terms of individual species both the model and observations show low NO$_x$ concentrations above 3 km, and the model tends to overpredict NO$_x$ in the boundary layer. The partitioning of nitric acid between the gas and particle phases remains a source of large uncertainty in atmospheric chemistry modeling. We present in Fig. 8f the total nitric acid calculated in the model expressed as the sum of gas phase nitric acid and the amount partitioned into the aerosol phase for C-130. The total predicted nitric acid is much closer to the observed gas phase nitric acid values, suggesting that the partitioning of nitric acid to the particle phase in the model may be overestimated (similar results are found for the DC-8, results not shown). Nitric acid predictions will be discussed further in Sect. 3.5.2.

The model overpredicts PAN at all altitudes by factors of ~1.5–2. Both the observations and the predictions show a very large variability in PAN at all altitudes, with ratios of the standard deviation to mean exceeding 1 (as shown in Fig. 8c). In previous evaluations of the STEM model over the western Pacific during TRACE-P, no such overprediction of PAN was found (Carmichael et al., 2003). During INTEX-B the sampled air was much more aged when compared to the TRACE-P. For these INTEX-B simulations we have found that the global model MOZART used to provide boundary conditions for these simulations overpredicted PAN by about factors of ~1.2–1.5 when compared directly with the aircraft observations (Fig. 8c). STEM predictions using these boundary conditions are shown to further increase PAN concentrations over those predicted by the global models. Similar results of greater net PAN production in the SAPRC-99 mechanism than in the MOZART chemistry are reported in Lin et al. (2010). The influence of different treatments of the boundary conditions on the STEM predictions has been reported previously (Tang et al., 2007). We performed additional calculations for this INTEX-B domain using two different global models (RAQMS and MOZART). The results show that long lived species distributions such as CO, PAN, and O$_3$ are sensitive to the boundary conditions, while short-lived species such as aerosol sulfate and nitrate are not.

The SAPRC-99 chemical mechanism used in STEM treats explicitly more organic peroxy radicals than many of the mechanisms used in global and regional atmospheric chemistry models. As such it tends to predict higher PAN levels. For example PAN calculations over Asia using SAPRC-99 were compared with identical simulations using the CB-IV mechanism by Lin et al. (2009, 2010). They found that SAPRC-99 produced 50 to 70% higher PAN levels over polluted regions. Recently, observations of a spectrum of acyl peroxy nitrates in the outflow of the Sacramento CA urban plume were compared with values calculated using a detailed chemical mechanism with features similar to those included
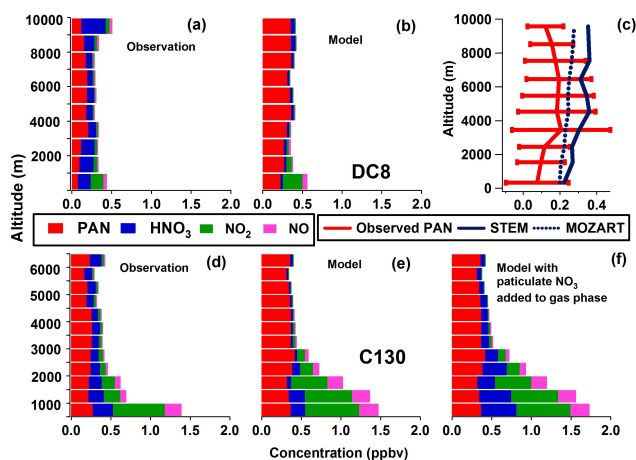
Fig. 8. Comparison of model predicted and observed NO_y components of DC-8 (top row) and C-130 (bottom row) during INTEX-B **(a)** DC-8 observed NO_y **(b)** DC-8 modeled NO_y **(c)** Vertical profile of DC-8 observed, STEM predicted and MOZART PAN **(d)** C-130 observed NO_y **(e)** C-130 modeled NO_y **(f)** C-130 modeled (NO_y + particulate NO_3).

Fig. 9. Comparison of STEM model predictions with DC-8 (top row) and C-130 (bottom row) observations of **(a)** DC-8 ozone photolysis rate (JO_3 s^{-1}) **(b, c)** DC-8 HO_x (OH and HO_2) species **(d, h)** DC-8 Formaldehyde (HCHO) **(e)** C-130 ozone photolysis rate (JO_3) **(f, g)** C-130 HO_x (OH and HO_2) species during INTEX-B. Note that panels (d, h) show two independent measurements of HCHO, which was only measured on the DC-8 aircraft for the INTEX-B period.

in SAPRC-99 (LaFranchi et al., 2009). They found that the model predictions exceeded the observations by factors of 2–5, with larger discrepancies at temperatures below 15 °C, which were attributed to current chemical mechanisms missing an important loss channel for the acyl peroxy radicals. Further research is needed to fully understand the causes of the overprediction of PAN.

To complete the evaluation of how well the model predicted important aspects of the photochemical oxidant cycle during the INTEX-B period we compare observed and predicted OH and the ozone photolysis rate constant (J-O_3) from the DC-8 and C-130 flights (Fig. 9). The modeled OH (Fig. 9b and f) shows a positive bias at lower altitudes and negative bias at high altitudes when compared to the DC-8 observations. Modeled OH values are more accurately predicted for the C-130 observations, but the predictions underestimate the variability in OH below 6 km for the C-130 (Fig. 9f) and overestimate it for the DC-8 (Fig. 9b). The overprediction of STEM modeled OH with the DC-8 observations may help explain some of the underprediction of CO in the DC-8 CO predictions (Fig. 7a and d) as discussed in Zhang et al. (2008), as the OH reaction removes CO from the atmosphere. The calculated J-O_3 rates (Fig. 9a and e) capture the observed vertical structure, but with a negative bias in the upper troposphere for the DC-8, and a much higher variability than observed. Above 5 km the RH values were also underpredicted (see Fig. 6c), and this coupled with the underprediction in J-O_3 can help explain the underprediction of OH above 5 km for the DC-8.

Predicted HO_2 vertical distributions (Fig. 9c and g) are consistent with the observed distributions for both the DC-8 and C-130, but with a systematic underprediction of both
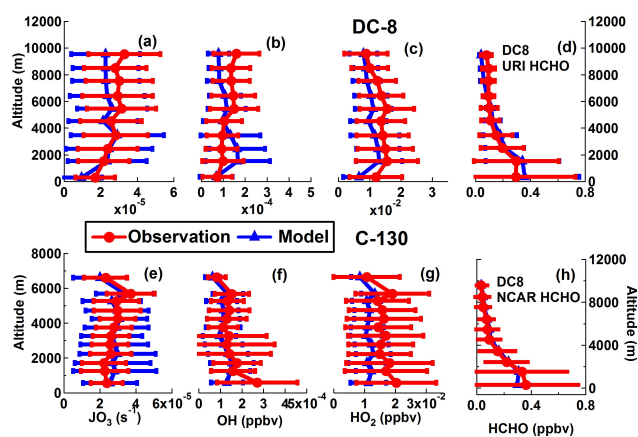
the magnitude and variability. HO_2 formation can be initiated by the reaction of CO with the OH radical, which also leads to the formation of hydrogen peroxide. Hydrogen peroxide is highly soluble in water and is therefore efficiently removed by wet deposition. Predicted values of hydrogen peroxide concentrations also show a negative bias, consistent with the underprediction in HO_2 (Figure not shown, statistics presented in Tables S1 and S2 of the supplemental materials http://www.atmos-chem-phys.net/10/2091/2010/acp-10-2091-2010-supplement.pdf).

Mao et al. (2008) analyzed the HO_x measurements from the DC-8 aircraft during the INTEX-B mission and compared the DC-8 airborne measurements with NASA Langley box model predictions of OH and HCHO. They also found an overprediction of OH in the boundary layer for the DC-8 flights and they related it to the underprediction of their modeled formaldehyde. There were two independent measurements of HCHO onboard the DC-8. We present our model comparisons with both sets of observations in Fig. 9d and h. The observations show a difference in the mean values, best illustrated by the boundary layer values. The model predictions fall between the two different sets of observations. Based on our model results we cannot discern whether the problem resides with HCHO as one of the measurement sets (i.e., NCAR-formaldehyde) seems to supports this hypothesis, while the other measurement set (i.e., URI-formaldehyde) does not. However, it must be kept in mind that the differences in the averages between the two HCHO measurements and between each measurement set and the model are all within the quoted measurement uncertainties.

3.3.3 Aerosols

Figure 10 presents the comparison of predicted and observed aerosols from the DC-8 and C-130. For the C-130 observations, we compare only to the AMS data, but Dunlea et al. (2009) showed that the AMS and PILS instrument measured similar concentrations of nitrate and sulfate for the INTEX-B study. Predicted sulfate is consistent with the DC-8 observed vertical structure (Fig. 10a), but with an underprediction in the mid-troposphere. For the C-130, the model fails to capture the elevated sulfate levels above 2 km that were observed by the C-130 (Fig. 10c). In addition the predicted variability is much lower than the observations. Evaluation of modeled SO_2 with both DC-8 and C-130 observations (Fig. S1 and Tables S1 and S2 of the supplemental materials) shows that SO_2 is systematically underpredicted by the model. Thus, it appears that the current SO_2 emission estimates are underestimated. SO_2 emissions in Asia grew significantly during this time period and while growth was accounted for in the INTEX-B emissions inventory, the growth could have been underestimated (Zhang et al., 2009). The nature of the pollutant transport in discrete plumes across the Pacific could also contribute to the underprediction of modeled SO_2 and sulfate. Dunlea et al. (2009) reported that for some of the flights during the INTEX-B period, the models missed the transport of large polluted air-masses that were so intense that missing these concentrations could easily modify the average vertical profiles of aerosols. As discussed further in Sect. 3.4.2 the predicted sulfate distribution does show an enhancement at these altitudes, but is greatly underestimated. But again the reason for the high sulfate in the C-130 flights that is not captured in the DC-8 observations remains an open question.

The model overpredicts nitrate aerosols in the lower altitudes for both the DC-8 and the C-130 (Fig. 10b and d). As shown in Fig. 8, the modeled HNO_3 gas phase values are underpredicted at low altitudes as well, but total nitrate (gas + particulate nitrate) is well captured. This suggests that the calculated partitioning into the particulate phase on dust, sea salt and potassium is too strong. Furthermore the large variability in the particulate nitrate is driven by the variability in the predicted dust, sea salt, and biomass burning aerosols.

While the AMS instrument onboard the C-130 measures organic aerosols, the STEM model in this application only calculated the concentration of primary organic carbon (OC). Thus, comparison of modeled OC with AMS organic matter (OM) is complex. To compare we converted AMS OM to OC with the OM/OC ratio of 1.9 (Dunlea et al., 2009) and which is consistent with values for rural and remote aerosols reported elsewhere (Turpin and Lim, 2001; Aiken et al., 2008), and found an underprediction, consistent with not accounting for SOA formation (e.g. Volkamer et al., 2006; Zhang et al., 2007; Hallquist et al., 2009). If we assume that the difference between the observed and predicted OC is due solely to secondary organic aerosol (SOA) and not other model er-
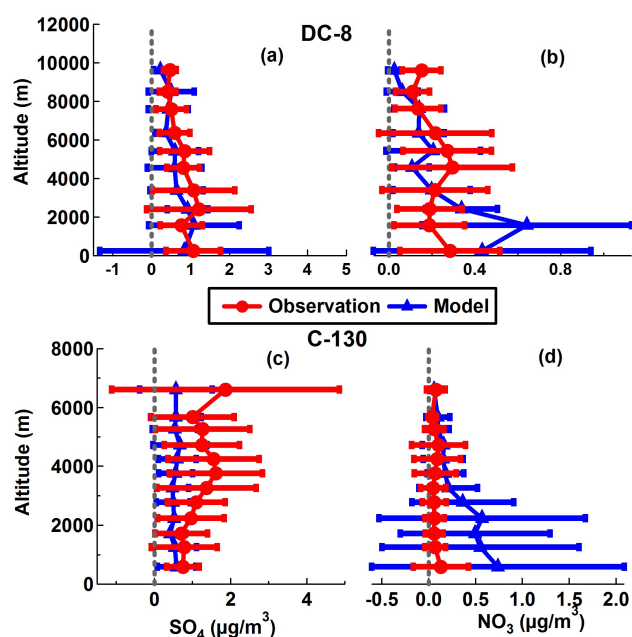

Fig. 10. Comparison of STEM model predictions versus observed aerosols from the DC-8 and C-130 **(a)** DC-8 Sulfate ($\mu g/m^3$) **(b)** DC-8 NO_3 ($\mu g/m^3$) **(c)** C-130 Sulfate ($\mu g/m^3$) and **(d)** C-130 NO_3 ($\mu g/m^3$).

rors such as emissions and removal processes, then SOA accounts for about 40% of the OC. The comparison of OM is given in Fig. S2 and Table S2 of the supplemental materials (see http://www.atmos-chem-phys.net/10/2091/2010/acp-10-2091-2010-supplement.pdf).

As a further evaluation of predicted distributions of aerosols in the study domain, we also compared predicted and observed mission-mean values at several surface sites including Kathmandu (KTM) Nepal and Trinidad Head (THD) from the ABC (Ramanathan et al., 2007) project and Cheju (CJU) South Korea and Oki (OKI) Japan from EANET network (EANET, 2006). These results in terms of $PM_{2.5}$, PM_{10}, sulfate and OC are presented in Fig. 11. These locations span the longitudes from 80° E to 120° W (Fig. 1a). Also included are results for the lowest 1 km DC-8 and C-130 flight segments. The predictions capture the strong gradient from west to east, with higher concentrations over the western portions of the model domain, but with a systematic negative bias.

3.4 Transpacific transport

3.4.1 Trajectory and source contribution analysis

In Fig. 12 we show five day three-dimensional back trajectories calculated using the WRF meteorology for points along the flight paths of selected flights. Three flights each from Hawaii (RF 11, 12, 13) and Alaska (RF 15, 16, 17) portions of the DC-8 mission and five C-130 (RF 15, 17, 18 21, 24)
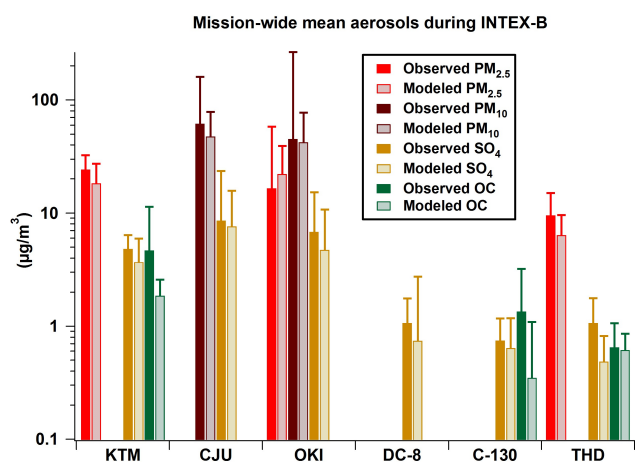
Fig. 11. Mission-wide mean aerosols at selected surface sites including Kathmandu (KTM) Nepal, Cheju (CJU) South Korea, Oki (OKI) Japan, and Trinidad Head (THD) US along with the DC-8 and C-130 data from all flights below 1 km a.s.l. during INTEX-B. Refer to Fig. 1 for the geographic location of the surface sites used in this figure.

flights that had substantial sampling over the eastern Pacific were chosen. The trajectories were initiated at the actual latitude, longitude, altitude and time of the airplane research flight segments. The trajectories were calculated along every minute of the flight path; however, to reduce the clutter trajectories are plotted only every thirty minutes.

The back trajectory analysis shows different transport patterns for the Hawaii, Alaska, and eastern Pacific portions of the INTEX-B mission. The Hawaii portion is dominated by air-masses passing over east central China reaching as far back as South Asia (Fig. 12a). In Fig. 12, air-mass back trajectories are colored by the altitude along the trajectory, and as expected the higher altitude air travels further reflecting the increase in wind speed with altitude. The back trajectories for the C-130 (Fig. 12c) show that the air-masses spent a substantial time over the Gulf of Alaska.

For each of these sets of research flights we extracted results from the tagged CO simulation to estimate how the source contributions varied by altitude. Results are presented in terms of % contribution from a specific source with respect to the total contribution from all the primary CO emission sources within the study domain (Fig. 12). For the Hawaii flights (Fig. 12b) we see that the biomass burning emissions from South/Southeast Asia has the largest impact at all altitudes. Emissions from China also have a significant impact (∼20%). The Alaska DC-8 flight segments (Fig. 12f) show the largest contribution from China emissions (∼40%), with fires from North Asia and South/Southeast Asia each contributing ∼20%. North America (NA) anthropogenic emissions are more significant in this region than for the Hawaii portion, reaching ∼15%. The majority of NA CO observed in this region is due to the NA CO transported globally and

brought back into the region via transport through the north and west boundaries. The results for the C-130 (Fig. 12d) fall between those for the Hawaii and Alaska portions. The contributions from South/Southeast Asia fires increase with altitude, while the importance of anthropogenic emissions from NA decrease with altitude. These contributions are generally consistent with the monthly mean distributions presented in Fig. 3, but with larger % contributions from biomass burning sources. This reflects the fact that the flights were designed to sample conditions most favorable to observing strong signatures of transpacific transport from Asia.

3.4.2 Air-mass age and aerosol processing

Figure 13 shows the mission-wide averages of calculated sulfate, potential sulfate (SO_2 + sulfate) and VOC age (Tang et al., 2004). The VOC age is a relative clock and gives qualitative information on the age of air-masses, and can be made more quantitative by calibration with other air-mass age indicators (e.g., trajectory analysis). These VOC ages represent clocks with respect to time inside the domain and the clock is set to zero for air-masses entering the domain through the boundaries; thus the VOC inferred ages of air-masses at the western boundary are less than ∼24 h. We present the results at 45° N latitude because most of the C-130 flights occurred between 40° N and 50° N as seen in Fig. 1b. From the VOC age distribution (Fig. 13 c) we see the dominant influence of westerly transport at all altitudes, with higher velocities at higher altitudes, as seen by the decrease in VOC age with increasing altitude. Air-masses at 160° W typically have ages on the order of 200 h, a duration similar to that found in previous studies (Jaffe et al., 1999; Reidmiller et al., 2009). The ∼200 h age contour provides a demarcation of regions heavily impacted by Asia outflow (to the west) and NA outflow (to the east). The NA outflow typically has ages <∼120 h at low altitudes (e.g., east of 120° W).

Sulfate (Fig. 13a) also shows a strong east to west gradient, with the highest concentrations over Central Asia (∼40° N) and East Asia as discussed earlier in association with Fig. 2. The Asian sulfate plume extends east to ∼140° W in the 3–7 km altitude range. In addition there is a second sulfate peak at similar altitudes around 130° W. This second peak occurs in very old air-masses (∼200 h) in association with elevated dust levels. This is a region that has contributions from China CO as well as contributions from Russia, North Asia biomass burning and South Asia biomass burning as shown in Fig. 3.

Sulfate is produced during the transpacific transport via chemical reactions with SO_2 that escapes the boundary layer in the source regions. This transformation can be tracked using the calculated sulfate to potential sulfate (i.e., the sum of sulfate plus SO_2 expressed as sulfate) ratio, which shows that the portion of available sulfur in the form of sulfate increases across the Pacific, consistent with SO_2 transformation to sulfate as it advects eastward to North America. Modeled results show that as air-masses approach the North American
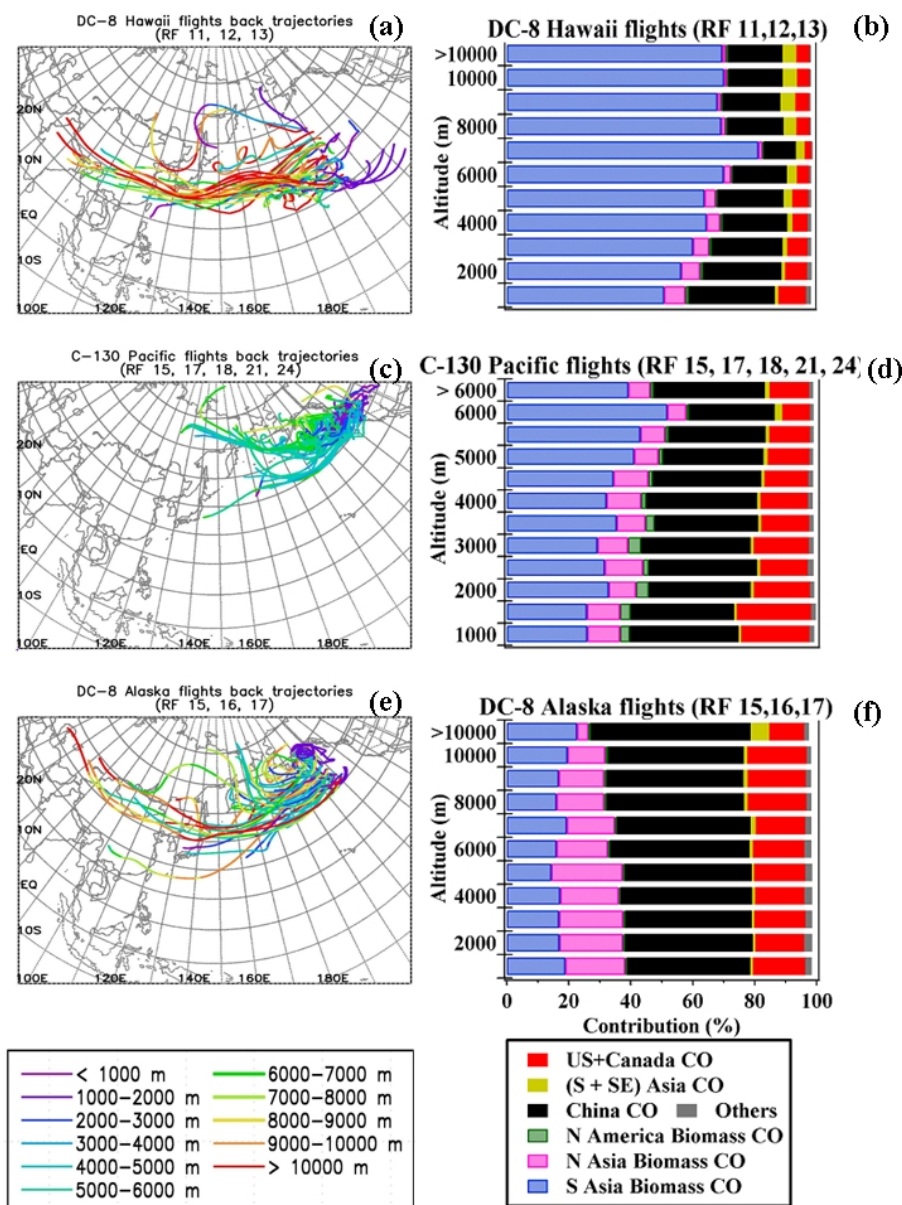
Fig. 12. Back trajectories of wind vectors and tagged anthropogenic/biomass CO tracers illustrating the source region of air-masses sampled by the selected DC-8 and C-130 flights. The back trajectories are colored by trajectory passing altitude and are plotted every 30 min along the DC-8/C-130 flight tracks. **(a)** DC-8 Hawaii flights (RF 11, 12, 13) back trajectories **(b)** Contribution of tagged anthropogenic/biomass CO tracers along the DC-8 Hawaii flights **(c)** C-130 Pacific flights (RF 15,17,18, 21, 24) back trajectories **(d)** Contribution of tagged anthropogenic/biomass CO tracers along the C-130 Pacific flights **(e)** DC-8 Alaska flights (RF 15, 16, 17) back trajectories (b) Contribution of tagged anthropogenic/biomass CO tracers along the DC-8 Alaska flights.

continent, the ratio of sulfate to potential sulfate decreases at the lower altitudes signifying the influence of North American SO_2 emissions on the air-mass (Fig. 13b). However we also see regions within the boundary layer extending from 130° W to 150° E with ratios greater than 0.8, reflecting the fact that air-masses reaching to near the surface can also have very long residence times. The sulfate to potential sulfate ratio represents another chemical clock, and it can be compared with the VOC age distribution (Fig. 13c). The distributions of VOC age and the ratio of sulfate to potential sulfate are similar east of 100° E. However west of 100° E the sulfate to potential sulfate ratio is large reflecting the differences in how the "clocks" were calculated, with the sulfate clock based on information provided through the boundary conditions and reflecting that the transport into the western boundary brings in air-masses high in sulfate and low in SO_2.

It is interesting to point out that the mean sulfate distribution does show an enhancement in sulfate at altitudes of 3–7 km, consistent with the C-130 observations, but it is much lower than observed. While the model extraction at the time and locations of the actual flights show only a slight enhancement in sulfate in the 2–7 km altitude range (Fig. 10c), a displacement of the predicted feature slightly to the west would be consistent with the observations. But again the magnitudes need to be much bigger, and most likely the emissions are underestimated.

We also examined the modeled OC to sulfate ratios as this has been discussed previously by Dunlea et al. (2009) and Peltier et al. (2008) for the same INTEX-B campaign. The OC to sulfate ratio reflects the differences in emissions, wet removal, and formation processes of these two types of aerosol. Dunlea et al. (2009) compared organic carbon (converted from OM measurements) ratio with AMS sulfate, while Peltier et al. (2008) examined the water soluble organic carbon (WSOC) with sulfate aerosols using their PILS instrument. STEM model results based on monthly mean OC and sulfate mixing ratios presented in Fig. 13d agree with Peltier et al. (2008) C-130 observations in that up to an altitude of ~3 km the ratio of OC/sulfate is about 1 or higher. As we follow the Asian air-mass (from VOC age or from the sulfate/potential sulfate ratios) we found that the ratio declines as we move up in altitude to values ~0.4, which is also consistent with the observations.

Both studies compared the aerosol ratios of organic carbon to sulfate with their own separate definitions of Asian air-mass origin to elucidate the transport and transformation of aerosols across the Pacific. Dunlea et al. (2009) identified air-masses of Asian origin using observed AMS sulfate >1 μg/m^3 and included only those data sampled by the C-130 west of 125° W . Peltier et al. (2008) screened data for Asian CO greater than 75% of the total anthropogenic FLEXPART CO as air-masses originating from Asia. The STEM predictions were examined using the data screening criteria defined by Dunlea et al. (2009). We also classified the STEM data similar to Peltier et al. (2008) study using predicted CO>100 ppb and tagged China anthropogenic CO>50% of the predicted total anthropogenic CO as screening criteria. Dunlea et al. (2009) showed that AMS and PILS instrument both showed similar results for sulfate concentration during the INTEX-B period. We used AMS sulfate and AMS OC (calculated from OM) data for comparison as it was readily available for both Peltier et al. (2008) and Dunlea et al. (2009) screening techniques mentioned above. The OC to sulfate ratios screened in these ways are shown in Fig. 14. Also shown are the OC to sulfate ratios for all the data points for the C-130 flights (no screening). Using all the data the OC to sulfate ratio is approximately 1 in the lowest 3 km, and drops to a value of ~0.3 between 3 and 6 km. The Peltier screening method shows a similar altitude dependency of the OC to sulfate ratio, with lower values (~0.6) in the lower altitudes. This is the result of their screening method that re-

moves some of the freshest air-masses from North America (which occur in the lowest 3 km and which have higher OC to sulfate ratios). The Dunlea screening method looks only at air-masses that have large enhancements of Asian pollution. It removes the North American air-masses as well as Asian air-masses that have low pollution contributions. Their results show a different vertical profile with the lowest values (<0.2) occurring near the surface and increasing to ~0.3 at 3 km. Above 3 km the value remains at ~0.3. At altitudes above 4 km all the profiles show that the ratio is on the order of 0.3–0.4.

The STEM predicted OC to sulfate ratio profiles for the various screening methods are also shown in Fig. 14. The magnitude of the OC/SO$_4$ ratio from the STEM predictions is larger than the corresponding observed AMS ratio. This may be due to the substantial underprediction of sulfate aerosol, although OC is also underpredicted as discussed above. The sulfate and OC profiles for the data screened by Dunlea et al. (2008) and Peltier et al. (2008) criteria are shown in Figs. S3 and S4 of supplemental materials (see http://www.atmos-chem-phys.net/10/2091/2010/acp-10-2091-2010-supplement.pdf). While the absolute ratios are biased high, the predicted profiles capture the important features of the observation based ratios. For example the impacts of the various screening methods on the profiles are clearly shown. The Peltier method results in a reduction of the ratios at all altitudes, with the greatest differences in the lower 2 km. The Dunlea screening results in a greater reduction in the ratios. These results can be understood in the context of the information presented in Fig. 13 and its discussion. Both screening techniques remove contributions of OC and sulfate of North American origin. The criteria used by Dunlea removes a substantially larger fraction of the North America contribution. The low values near the surface in the Dunlea screening is due to the fact that these observation points are very aged as reflected in the monthly mean air-mass age distributions shown in Fig. 13c. These results support the idea that the OC to sulfate ratio is lower in more aged air-masses. However, these results should be interpreted cautiously, as Peltier et al. (2008) compared WSOC/sulfate ratios while we compared OC/sulfate ratios.

3.4.3 Influence of transpacific transport on the western US

There is currently keen interest in evaluating the importance of intercontinental transport of pollution (NRC, 2009; HTAP, 2007). Observations of trace gases and aerosols were also available from the surface site at Mt. Bachelor Observatory (MBO, 44.0° N, 121.7° W) in Oregon. Observations at MBO have been shown to be particularly useful in studying long range transport (Jaffe et al., 1999; Wolfe et al., 2007; Reidmiller et al., 2009). Here we analyze the MBO data with respect to the INTEX-B conditions. The comparison of predicted ozone and PAN with measurements from MBO during
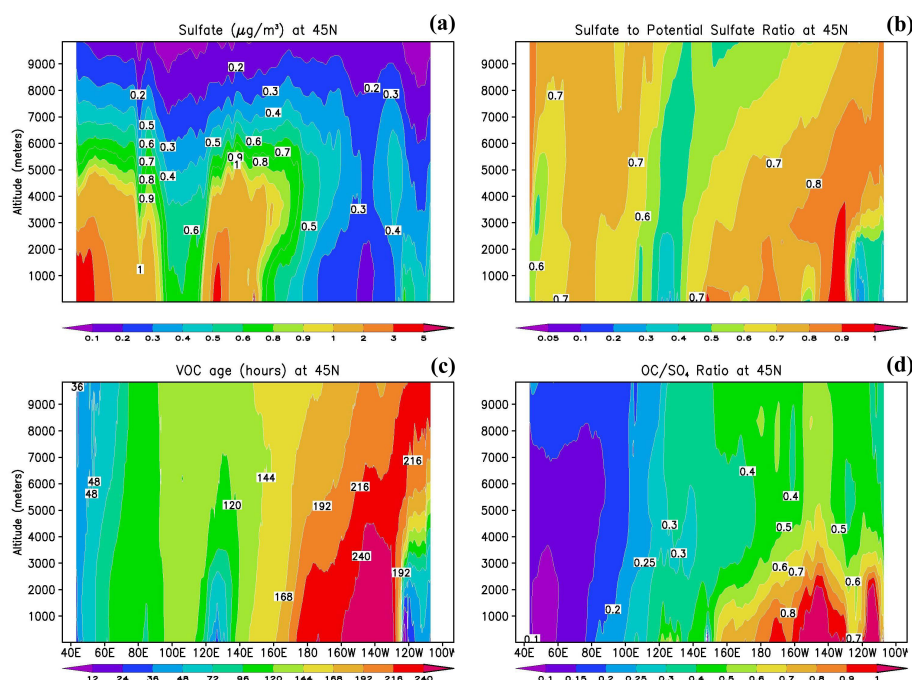
Fig. 13. Mission wide average meridonial cross sections of aerosols at 45° N during INTEX-B **(a)** Sulfate **(b)** Sulfate to Potential Sulfate ratio **(c)** VOC age (hours) and **(d)** OC/SO₄ ratio. The values on the cross section plots denote the contour labels at sharp gradients.
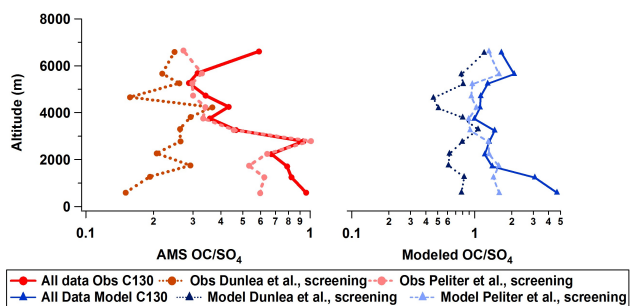

Fig. 14. Average vertical profiles of OC/SO$_4$ ratio during the INTEX-B campaign. The observed OC/SO$_4$ ratio is calculated using the OC (OM/1.9) and SO$_4$ measurements from AMS aboard the C-130 aircraft. The Dunlea et al. (2008) screening criteria are Observed AMS SO$_4$ > 1 μg/m^3 and sampled west of 125° W longitude. The Peltier et al. (2008) criteria used are modeled CO > 100 ppb and model tagged China anthropogenic CO > 50% of the predicted total anthropogenic CO.

the INTEX-B is shown in Fig. 15d. The model is able to capture both the magnitude as well as the temporal trends of ozone and PAN. It is important to note that modeled PAN is much closer in agreement to the measurements at MBO than when compared to the airborne DC-8 and C-130 measurements. This may be due to the fact that regional production of PAN plays a larger role and that the emissions over NA are better characterized than over Asia. We also show calculated vertical distributions as a function of time

for ozone (Fig. 15a), PAN (Fig. 15b) and dust (Fig. 15c). Dust is a good tracer for transpacific transport during this period as this is a period of active dust emissions in Asia. The vertical distribution of dust (Fig. 15c) over MBO shows that dust events occur on synoptic time scales, and pass over this location between 3–7 km a.g.l. altitudes. Dust reaches the surface in subsiding air-masses through entrainment into the boundary layer as shown on 11 May. The ozone curtain shows high variability in the upper altitudes with influence of stratospheric ozone as well as from long range transport (Fig. 15a). The PAN vertical structure shows the influence of local sources as well as elevated plumes associated with long range transport (Fig. 15b). There are periods when ozone and PAN are not correlated, but more periods when they are correlated showing that long range transport in the upper troposphere during this period brings together air masses of widely different origins. This is also shown by the dust distribution correlations with ozone, which occurs in the dust source regions wherein the low pressure systems bring dust up from the surface and ozone down from high altitudes. The patterns show differences and similarities in the vertical structures between these three components, and these illustrate the complexities in the processes at play during the long range transport over the Pacific. The superimposed time series of modeled surface level dust, ozone and PAN (Fig. 15d) further illustrates the different characteristics of these three constituents. For example, the ozone peak on the 22 April is associated with relatively low PAN (with peak
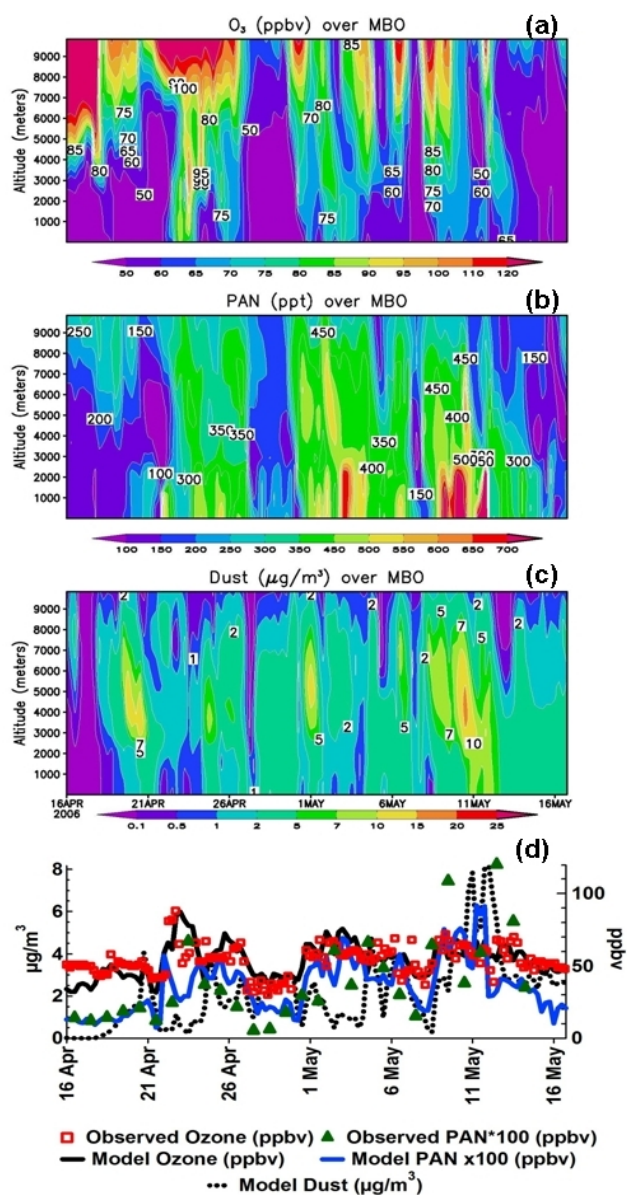
Fig. 15. (a) Time altitude cross sections of trace gases at MBO during INTEX-B (a) ozone (ppb) **(b)** PAN (ppt) **(c)** Dust (µg/m³) **(d)** Comparison of observed and modeled ozone and PAN at the surface. Note that panel (d) also includes the modeled dust. The values on the cross section plots denote the contour labels at sharp gradients.

ozone being anti-correlated with PAN), and low dust values. The peak around 3 May has both high ozone and PAN but low dust concentration. Finally the peak around 11 May has high ozone, dust and PAN.

To help put these three periods in perspective modeled ozone, PAN and dust distribution at 3 km a.g.l. at 18 Z for 22 April, 3 May and 11 May are shown in Fig. 16. Wind barbs are also plotted in these figures to illustrate the transport patterns. On 22 April, modeled ozone (Fig. 16a) is high over

MBO along the eastern side of the ridge bringing descending air of stratospheric origin from the North. The ridge clearly separates the ozone transported from Asia which is on the western side of the ridge. Thus the air over MBO has high ozone and low dust as shown clearly in the vertical profiles of Fig. 15. On 3 May (Fig. 16c), there is another weak ridge over the eastern Pacific which transports pollution from the North. This ridge is not as strong as on 22 April. To the east of the ridge ozone and PAN are correlated, with maximum values at the surface, and moderate values aloft. Dust values at the surface remain low, reflecting the lack of local emissions and wet removal along its transport path. The third pollutant peak over MBO around 11 May (Fig. 16e) shows zonal flow transporting dust, ozone, PAN and other pollutants from Asia to the west coast of the US.

To further understand the flow characteristics of these three events, we estimated ozone/PAN/dust distributions backward in time by combining the corresponding observed values at MBO with air-mass back trajectories. For this analysis, we used three-dimensional 12 day backward trajectories calculated from the model to assess the impact of long range transport over MBO. The location of an air parcel at a particular time was represented by the trajectory segment latitude and longitude endpoints. The entire geographic region covered by the trajectories was divided into an array of grid cells. It was assumed that the concentration did not change from the value observed at MBO for a particular time along the back trajectories. Let $m_{i,j}$ be the number of segment endpoints in i, j^{th} grid cell that denote the trajectories arriving at MBO when the time corresponds to a particular pollution event described above. The average concentration of each grid cell $C_{i,j}$ was calculated by using the Eq. (1):

$$C_{i,j} = \frac{1}{m_{i,j}} \sum_{k=1}^{m_{i,j}} C_k \quad (1)$$

where C_k denotes the observed concentration at the time when the back trajectory was initialized. Thus the concentration of species was reconstructed along the path of back trajectories. Further details are described elsewhere (Kurata et al., 2004). The trajectories were colored by the mean observed pollutant concentration associated with them and these results are also shown in Fig. 16. The reconstructed concentration plot of ozone along the trajectory path for the first event around 22 April clearly shows the path of the high ozone (Fig. 16b, grid cells colored in red) coming from the north with relatively lower values along the direct Asian transport path. Similar plots for PAN and dust (not shown) show low values consistent with the above findings. Likewise, the plot of PAN for the event on 3 May shows that high values of PAN (Fig. 16d) and ozone (not shown) with relatively lower dust (not shown) originate along the path coming from the north/northwest direction. Finally for the peak on May 11, the dust plot (Fig. 16f) clearly shows that the high
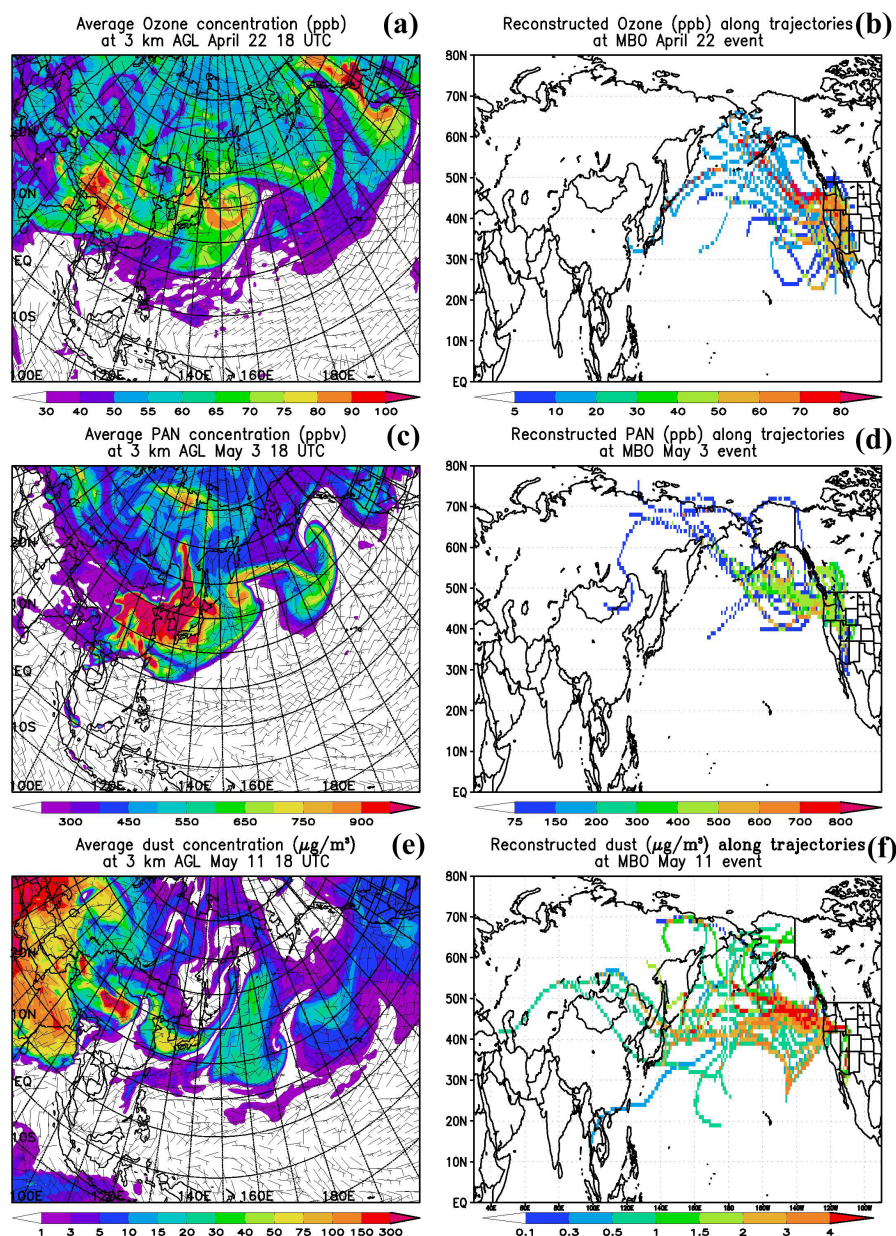
Fig. 16. Horizontal distribution of modeled ozone, PAN, and dust at 18 z, 3 km a.g.l. layer along with redistributed concentration along back trajectories on 22 April **(a, b)**, 3 May **(c, d)** and 11 May **(e, f)** during INTEX-B.

values of dust, along with PAN and ozone (not shown) are transported along the zonal flow originating from Asia.

We also analyzed the CO observations at MBO (Fig. 17). The observed and predicted CO concentrations at the surface at MBO are shown in Fig. 17d. At the start of the time series both the model and the observations show very small variability, but the model shows a systematic offset. We do not have a clear explanation for this, but as it was a period of prolonged high concentrations in the observations, it could be do to a biomass emission issue that is not captured in our

model. After the initial few days, the predicted values capture the magnitude and much of the observed variability with some offsets in timing and magnitude, which may be in part due to the resolution of the model and displacements in the flow fields.. An exception being that the model overestimates the peak on 11 May. We investigated this further by using the results from the tagged-CO tracer simulation to estimate the contribution of different emission sources and regions at MBO. Time series of source region tagged CO over MBO at 5.3 km a.g.l. and at the surface are also shown (Fig. 17b

and c). Connecting these two figures, we show the modeled CO curtain over MBO (Fig. 17a). At the surface (Fig. 17c) the predicted CO levels are influenced by NA emissions, as well as by emissions from China and South/Southeast Asia fires. NA fires also contribute at discrete times. For example the predicted peak on 11 May is not seen as out of the ordinary in the observations. The model attributes this to a biomass plume from North America, which is not obvious from the observations. The contribution from US/Canada sources at the surface show clearly a small diurnal cycle associated with boundary layer processes and up-slope and down-slope winds. Even at the surface the contribution from distant sources is approximately 50%. At 5.3 km a.g.l. (Fig. 17b) the contributions from China and South/Southeast Asia fire emissions grow in importance. The largest contributions from China and North Asia fire emissions occur around 11 May, a period that also had high dust amounts as discussed earlier.

3.5 The impact of aerosols on tropospheric chemistry over the Pacific Ocean

During the INTEX-B experiment the aerosol loadings in the domain were often quite high due to anthropogenic emissions and emissions from biomass burning and wind blown dust. Aerosols can impact the atmospheric chemistry through a variety ways, including altering photolysis rates and through heterogeneous reactions on particle surfaces. We have previously shown that in the East Asia outflow these effects can be large (Tang et al., 2003, 2004b). We performed additional calculations to evaluate the effects of aerosols during the INTEX-B period. In one experiment we turned off the effect of aerosols in the TUV photolysis model (i.e. made the aerosol concentration values equal to zero in the TUV subroutine). Figure 18 shows the percent change in the mean concentrations of OH, ozone, NO_x and sulfate aerosol due to changes in the photolysis rate calculation for the Hawaii portion (16–30 April) of the INTEX-B campaign. Our results show that aerosols strongly influence the chemistry of short lived species like OH and NO_x over the polluted regions of Asia and the western Pacific. In East Asia the OH values on averaged decrease and NO_x levels increase by 20 to 30% due to the effects of aerosols on the photolysis rates, which in turn impact sulfate and ozone, resulting in decreases in the aerosol laden air-masses by ~5%. An important component in the calculated variability in the photolysis rates discussed earlier in the paper is due to the variability in the predicted aerosol mass and its vertical distribution. This can be seen in the large variability in the predicted particulate nitrate (Fig. 10), which reflects the variability in the dust, sea salt and biomass burning aerosols. The other major component is the variability in the predicted clouds.

We also examined the importance of heterogeneous chemistry on the trace species distributions during INTEX-B. Heterogeneous chemistry on dust surfaces was shown to be im-
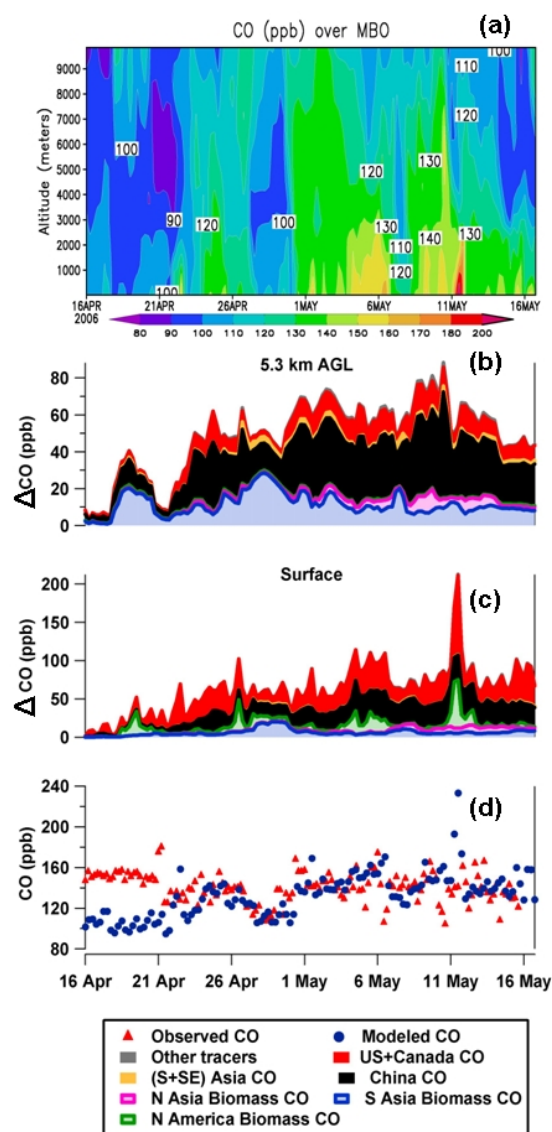

Fig. 17. (a) Time altitude cross section of CO, time series of source region tagged CO tracers at (b) 5.3 km a.g.l. (c) surface along with the (d) comparison of observed and modeled CO at MBO during INTEX-B. The values on the CO cross section plot denote the contour labels at sharp gradients.

portant during the 2001 NASA TRACE-P and ACE-Asia field campaigns by Tang et al. (2004b). An additional simulation was performed where the reactions of ozone, SO_2 and NO_2 and HNO_3 on dust were turned off. The change in trace species distributions are presented in Fig. 19. In the East Asia outflow the impact of heterogeneous reactions on dust is significant, increasing the average aerosol sulfate and nitrate by up to 10% and 20%, respectively, while reducing ozone levels by 5 to 10%. Over the central and eastern Pacific, where the INTEX-B flights were conducted, the mean impacts of the heterogeneous reactions on dust for sulfate and
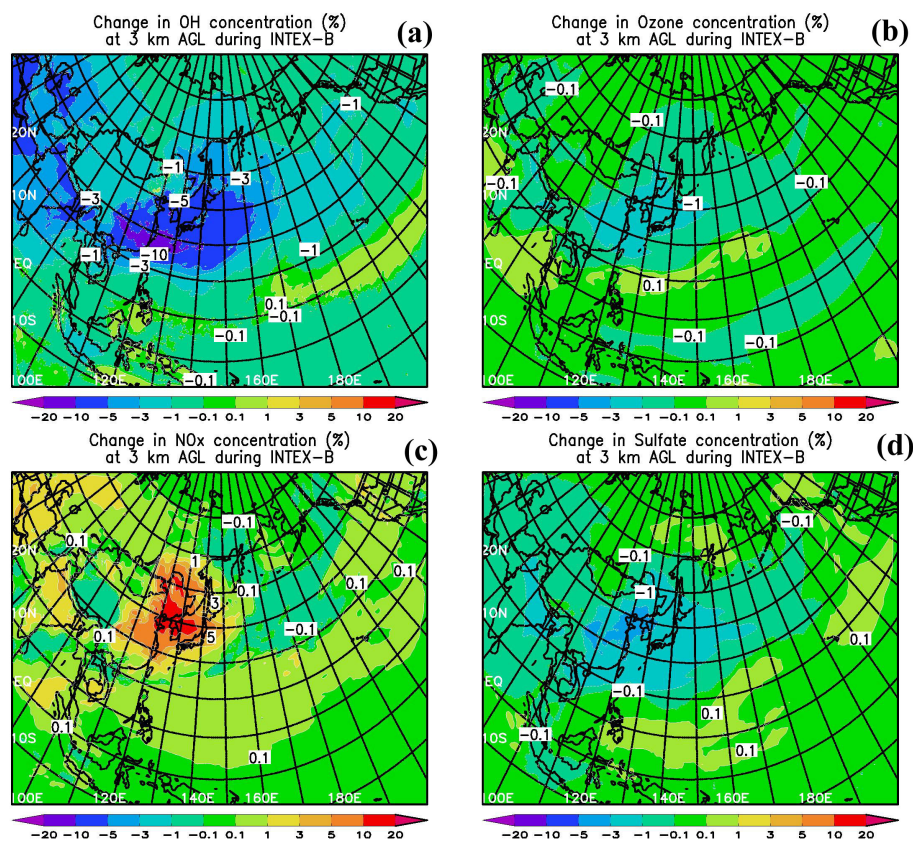
Fig. 18. Average percent change in the concentration of trace gases and aerosols without the contribution of aerosols in photolysis rate calculation during the Hawaii portion of INTEX-B **(a)** OH **(b)** Ozone **(c)** NO_x and **(d)** Sulfate. Shown are ((with aerosol – without aerosol)/without aerosol)·100. The values on the maps denote the contour labels at sharp gradients.

nitrate were 1–5%. These mean effects are smaller than those found for the TRACE-P/ACE-Asia experiments by Tang et al. (2004b). This reflects the fact that the INTEX-B period of April/May 2006 had lower dust levels than the March/April period of 2001, and that the flight operations were conducted over the eastern Pacific, far away from the outflow regions sampled during TRACE-P/ACE-Asia experiments.

However the impacts of the heterogeneous reactions at specific times during dust transport episodes can be much larger than the mean impacts discussed above. McNaughton et al. (2009) analyzed the aerosol and gas phase measurements on the DC-8 aircraft to show that in the presence of dust both sulfate and nitrate aerosol production is increased, and that as a result of the dust reactions, gas phase nitric acid levels are reduced appreciably. In Fig. 20a we show plots of observed sulfate to total potential sulfate (sum of sulfate and SO_2) as a function of aerosol Ca for all DC-8 flights, for altitudes above 1.5 km, CO and O_3 greater than 90 and 40 ppb, respectively, and ^7Be less than 800 fCi s/m^3 to exclude data influenced by clean air-masses and stratosphere. The data points show an envelope, with the ratio increasing with increases in Ca. Also shown are the predicted values for the same ratio plotted as a function of predicted dust concentra-

tion. The model shows a very similar behavior (Fig. 20b) as that based on the observations. In Fig. 20c and d, we plot the observed and modeled ratio of particulate nitrate to total nitrate (sum of particulate nitrate and gaseous nitric acid). Observations show that for Ca concentrations above ~0.5 µg/m^3, the nitric acid partitions into the dust, reducing the gas phase concentrations by ~50% (as discussed further in McNaughton et al., 2009). The model shows qualitatively a similar behavior.

These results show that aerosol interactions can play important roles in the atmospheric chemistry over the Pacific. The results also show that there remain large uncertainties in the modeling of these interactions. This was illustrated by the comparisons of predicted HNO$_3$ and particulate nitrate with observations which showed that the model appears to overestimate the partitioning into the aerosol phase. Further guidance is needed from laboratory studies to help improve the model treatment of heterogeneous chemistry on ambient aerosol.
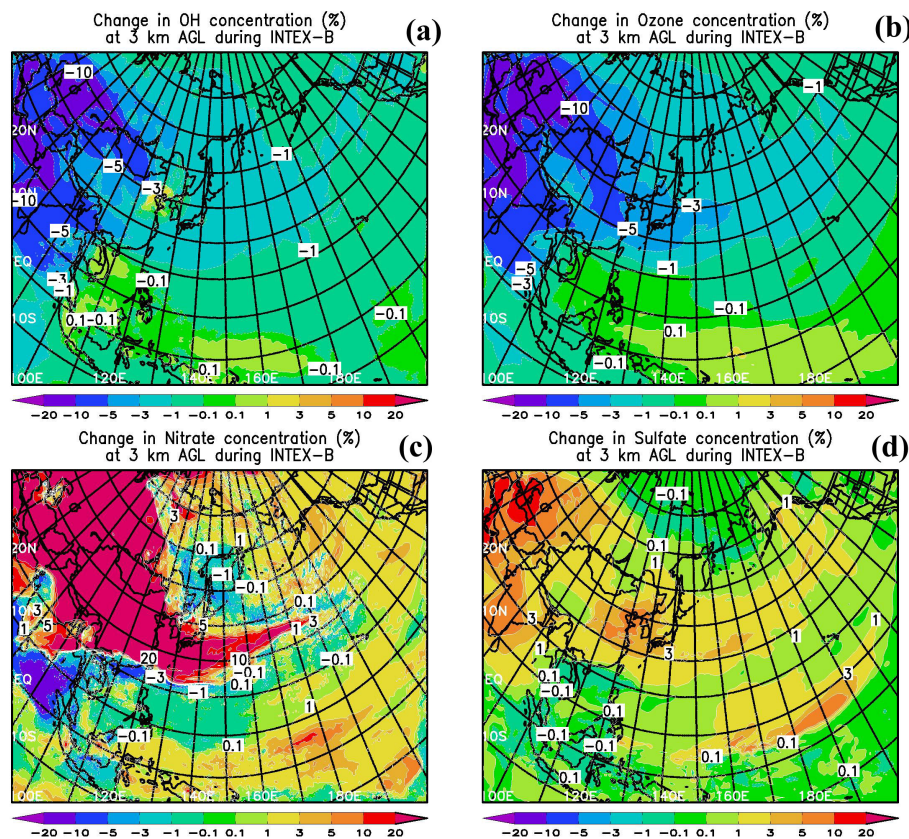
Fig. 19. Average percent change in the concentration of trace gases and aerosols without heterogeneous chem. during the Hawaii portion of INTEX-B **(a)** OH **(b)** Ozone **(c)** Nitrate and **(d)** Sulfate. Shown are ((heterogeneous − without heterogeneous)/without heterogeneous)·100. The values on the maps denote the contour labels at sharp gradients.

4 Summary

The STEM regional chemical transport model was used to simulate the distributions of trace gases and aerosols over the Pacific during the April/May 2006, which was the time period of the INTEX-B experiment. This was a period with active biomass burning emissions in South/Southeast Asia, North Asia and North America, active wind blown dust events, and strong westerly flows. As a result pollutants were transported into and across the Pacific. Trace species distributions show strong west (high) to east (low) gradients, with the bulk of the pollution transport over the central Pacific occurring between ~20° N and 50° N at altitudes between ~2 and 6 km.

The modeled fields over the eastern Pacific were evaluated using the observations from the NASA INTEX-B field campaign. Thirty different meteorological, trace gas and aerosol parameters were compared. The STEM chemical transport was driven by the recently developed Weather Research and Forecast (WRF) meteorological model. The WRF model was found to do a good job in capturing main features of the meteorology over the eastern Pacific in terms of wind speed and direction, temperature and relative humidity. In general the meteorological fields were better predicted than gas phase species, which in turn were better predicted than aerosol quantities. Despite successfully predicting many of the measured parameters, the results identified areas where prediction improvements are needed. For example the predicted CO enhancements were underpredicted over the central Pacific; mostly likely cause is that the emissions from anthropogenic and open burning sources were underestimated during this time period. Other issues point to potential structural problems in our models. For example PAN was significantly overpredicted over the eastern Pacific. This was attributed to uncertainties in the chemical mechanisms used in current atmospheric chemistry models in general, and specifically to the high PAN production rates in the SAPRC-99 mechanism used in our regional model. The systematic underprediction of the elevated sulfate layer in the eastern Pacific observed by the C-130 was another problem identified. While the model predicts such an enhancement at altitudes between 3 and 6 km, it was significantly underestimated. At this point we do not know whether this is a problem with the SO_2 emissions in the region, or some other process in the model (such as wet removal).
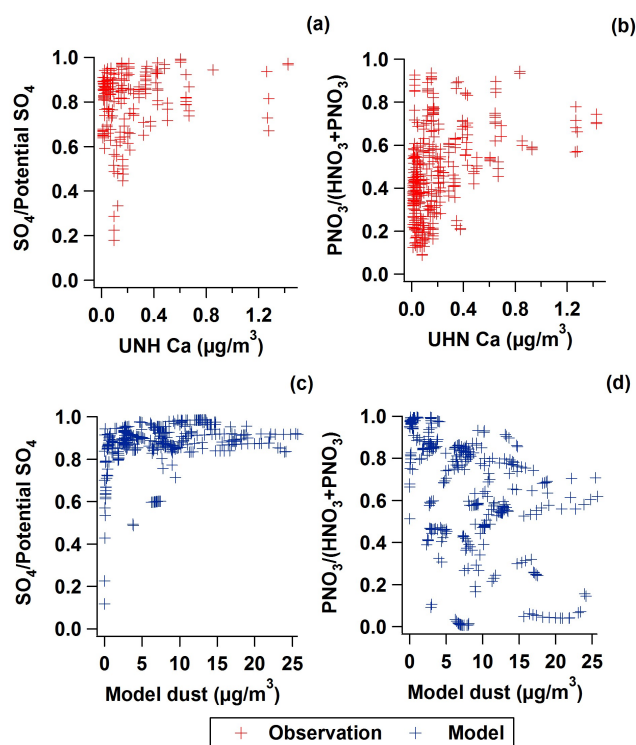
Fig. 20. Comparison of model predicted ratios with DC-8 observations **(a)** observed SO_4/Potential SO_4 ratio **(b)** observed aerosol NO_3/(aerosol NO_3+HNO_3) **(c)** Modeled SO_4/Potential SO_4 ratio **(d)** Modeled aerosol NO_3/(aerosol NO_3+HNO_3).

An analysis of the impact of various source regions of anthropogenic and biomass burning emissions on the trace distributions over the Pacific and for specific flight segments was performed using tagged CO experiments. During this period the largest contributions were from China and from fires in South/Southeast Asia and North Asia. These source regions impacted the distributions over the Pacific in different ways. For example, it was found that for the Hawaii flights the biomass burning emissions from Southeast Asia had the largest impact at all altitudes (45–70%), with emissions from China contributing ∼20%. The Alaska DC-8 flight segments showed the largest contribution from China emissions (∼40%), with fires from North Asia and South/Southeast Asia each contributing ∼20%. North America anthropogenic emissions were more significant in this region than for the Hawaii portion, reaching ∼15%. The results for the C-130 segments, which operated farther to the east and at latitudes between those for the above cases, fell between those for the Hawaii and Alaska portions. The transport of pollution into the western US was studied through an analysis of the observations at the Mt. Bachelor Observatory (MBO). This high altitude station was found to see a variety of influences during the INTEX-B period, including events with elevated Asia dust, and periods with contributions from China and fires from both Asia and North America.

The impact of heterogeneous chemistry on dust surfaces was also evaluated. The results showed that these mechanisms are important and in dust laden air-masses can enhance the production of aerosol sulfate and nitrate, and significantly reduce the nitric acid concentrations over the central and eastern Pacific. Modeled results showed that while aerosol impacts on photolysis rates were important over the source region, they were not significant over the central and eastern Pacific. The results also showed that there remain large uncertainties in the modeling of these interactions. This was illustrated by comparisons of predicted HNO_3 and particulate nitrate with observations, which showed that the model appears to overestimate the partitioning into the aerosol phase. Further guidance is needed from laboratory studies to help improve the model treatment of heterogeneous chemistry on ambient aerosol.

Finally these results show that chemical transport models provide an important tool for the analysis of comprehensive data sets such as those obtained in INTEX-B. However there remain important limitations as discussed above. Further improvements in the models will require better estimates of emissions, a better understanding of aerosol-gas phase interactions, and a better understanding of the root causes of errors in the prediction of important aspects of the photochemical processes.

Edited by: L. Molina

References

Aiken, A. C., DeCarlo, P. F., Kroll, J. H., et al.: O/C and OM/OC Ratios of Primary, Secondary, and Ambient Organic Aerosols with High Resolution Time-of-Flight Aerosol Mass Spectrometry, Environ. Sci. Technol., 42, 4478–4485, doi:10.1021/es703009q, 2008.

Al-Saadi, J., Soja, A. J., Pierce, R. B., Szykman, J., Wiedinmyer, C., Emmons, L., Kondragunta, S., Zhang, X., Kittaka, C., Schaack, T., and Bowman, K.: Intercomparison of near-real-time biomass burning emissions estimates constrained by satellite fire data, J. Appl. Remote Sens., 2, 021504–021524, 2008.

Bertschi, I. T., Jaffe, D. A., Jaegle, L., Price, H. U., and Dennison, J. B.: PHOBEA/ITCT 2002 airborne observations of transpacific transport of ozone, CO, volatile organic compounds, and aerosols to the northeast Pacific: Impacts of Asian anthropogenic and Siberian boreal fire emissions, J. Geophys. Res., 109, D23S12, doi:10.1029/2003JD004328, 2004.

Bey, I., Jacob, D. J., Logan, J. A., and Yantosca, R. M.: Asian chemical outflow to the Pacific in spring: Origins, pathways, and budgets (vol. 106, p. 23097, 2001), J. Geophys. Res.-Atmos., 108, 4162, doi:10.1029/2003JD001603, 2003.

Carmichael, G. R., Peters, L. K., and Kitada, T.: A 2nd Generation Model for Regional-Scale Transport Chemistry Deposition, Atmos. Environ., 20, 173–188, 1986.

Carmichael, G. R., Peters, L. K., and Kitada, T.: A 2nd Generation Model for Regional-Scale Transport Chemistry Deposition, Atmos. Environ., 20, 173–188, 1986.

Carmichael, G. R., Tang, Y., Kurata, G., Uno, I., Streets, D., Woo, J. H., Huang, H., Yienger, J., Lefer, B., Shetter, R., Blake, D., Atlas, E., Fried, A., Apel, E., Eisele, F., Cantrell, C., Avery, M., Barrick, J., Sachse, G., Brune, W., Sandholm, S., Kondo, Y., Singh, H., Talbot, R., Bandy, A., Thorton, D., Clarke, A., and Heikes, B.: Regional-scale chemical transport modeling in support of the analysis of observations obtained during the TRACE-P experiment, J. Geophys. Res.-Atmos., 108, 8823, doi:8810.1029/2002JD003117, 2003.

Carter, W. P. L.: Development and evaluation of the SAPRC-99 chemical mechanism, final report to California Air Resources Board, Air Pollution Research Center and College of Engineering Center for Environmental Research and Technology, University of California, Riverside, CA, USA, Contract No. 92–329, 2000.

Dunlea, E. J., DeCarlo, P. F., Aiken, A. C., Kimmel, J. R., Peltier, R. E., Weber, R. J., Tomlinson, J., Collins, D. R., Shinozuka, Y., McNaughton, C. S., Howell, S. G., Clarke, A. D., Emmons, L. K., Apel, E. C., Pfister, G. G., van Donkelaar, A., Martin, R. V., Millet, D. B., Heald, C. L., and Jimenez, J. L.: Evolution of Asian aerosols during transpacific transport in INTEX-B, Atmos. Chem. Phys., 9, 7257–7287, 2009, http://www.atmos-chem-phys.net/9/7257/2009/.

EANET (2006): EANET Data on the Acid Deposition in the East Asian Region, online available at: http://www.eanet.cc/product/datarep/datarep06/datarep2006.pdf, 2006.

Forster, C., Cooper, O., Stohl, A., Eckhardt, S., James, P., Dunlea, E., Nicks Jr., D. K., Holloway, J. S., Hubler, G., Parrish, D. D., Ryerson, T. B., and Trainer, M.: Lagrangian transport model forecasts and a transport climatology for the Intercontinental Transport and Chemical Transformation 2002 (ITCT 2K2) measurement campaign, J. Geophys. Res., 109, D07S92, doi:10.1029/2003JD00358, 2004.

Fuelberg, H. and Latto, A.: Quasi-Lagrangian Sampling during INTEX-B, online available at: http://fuelberg.met.fsu.edu/research/intexb/intersect/desc.html, 2008.

Garg, A., Shukla, P. R., and Kapshe, M.: The sectoral trends of multigas emissions inventory of India, Atmos. Environ., 40, 4608–4620, 2006.

Gong, S. L.: A parameterization of sea–salt aerosol source function for sub- and super-micron particles, Global Biogeochem. Cy., 17, 1097, doi:1010.1029/2003GB002079, 2003.

Grassian, V. H.: Chemical reactions of nitrogen oxides on the surface of oxide, carbonate, soot, and mineral dust particles: Implications for the chemical balance of the troposphere, J. Phys. Chem. A, 106, 860–877, 2002.

Hadley, O. L., Ramanathan, V., Carmichael, G. R., Tang, Y., Corrigan, C. E., Roberts, G. C., and Mauger, G. S.: Trans-Pacific transport of black carbon and fine aerosols ($D < 2.5\,\mu m$) into North America, J. Geophys. Res.-Atmos., 112, D05309, doi:05310.01029/02006JD007632, 2007.

Hallquist, M., Wenger, J. C., Baltensperger, U., Rudich, Y., Simpson, D., Claeys, M., Dommen, J., Donahue, N. M., George, C., Goldstein, A. H., Hamilton, J. F., Herrmann, H., Hoffmann, T., Iinuma, Y., Jang, M., Jenkin, M. E., Jimenez, J. L., Kiendler-Scharr, A., Maenhaut, W., McFiggans, G., Mentel, Th. F., Monod, A., Prévôt, A. S. H., Seinfeld, J. H., Surratt, J. D., Szmigielski, R., and Wildt, J.: The formation, properties and impact of secondary organic aerosol: current and emerging issues, Atmos. Chem. Phys., 9, 5155–5236, 2009, http://www.atmos-chem-phys.net/9/5155/2009/.

Hemispheric Transport of Air Pollution 2007: United Nations Economic Commission for Europe, New York and Geneva, online available at: http://www.htap.org/, 2007.

Jacob, D. J., Crawford, J. H., Kleb, M. M., Connors, V. S., Bendura, R. J., Raper, J. L., Sachse, G. W., Gille, J. C., Emmons, L., and Heald, C. L.: Transport and Chemical Evolution over the Pacific (TRACE-P) aircraft mission: Design, execution, and first results, J. Geophys. Res.-Atmos., 108, 1–19, 2003.

Jaffe, D., Anderson, T., Covert, D., Kotchenruther, R., Trost, B., Danielson, J., Simpson, W., Berntsen, T., Karlsdottir, S., Blake, D., Harris, J., Carmichael, G., and Uno, I.: Transport of Asian air pollution to North America, Geophys. Res. Lett., 26, 711–714, 1999.

Kim, Y. P. and Seinfeld, J. H.: Atmospheric Gas–Aerosol Equilibrium 3, Thermodynamics of Crustal Elements Ca2+, K+, and Mg2+, Aerosol Sci. Technol., 22, 93–110, 1995.

Kurata, G., Carmichael, G. R., Streets, D. G., Kitada, T., Tang, Y., Woo, J. H., and Thongboonchoo, N.: Relationships between emission sources and air-mass characteristics in East Asia during the TRACE-P period, Atmos. Environ., 38, 6977–6987, 2004.

LaFranchi, B. W., Wolfe, G. M., Thornton, J. A., Harrold, S. A., Browne, E. C., Min, K. E., Wooldridge, P. J., Gilman, J. B., Kuster, W. C., Goldan, P. D., de Gouw, J. A., McKay, M., Goldstein, A. H., Ren, X., Mao, J., and Cohen, R. C.: Closing the peroxy acetyl nitrate budget: observations of acyl peroxy nitrates (PAN, PPN, and MPAN) during BEARPEX 2007, Atmos. Chem. Phys., 9, 7623–7641, 2009, http://www.atmos-chem-phys.net/9/7623/2009/.

Lathière, J., Hauglustaine, D. A., Friend, A. D., De Noblet-Ducoudré, N., Viovy, N., and Folberth, G. A.: Impact of climate variability and land use changes on global biogenic volatile organic compound emissions, Atmos. Chem. Phys., 6, 2129–2146, 2006, http://www.atmos-chem-phys.net/6/2129/2006/.

Levy, H., Schwarzkopf, M. D., Horowitz, L., Ramaswamy, V., and Findell, K. L.: Strong sensitivity of late 21st century climate to projected changes in short-lived air pollutants, J. Geophys. Res.-Atmos., 113, D06102, doi:06110.01029/02007JD009176, 2008.

Liang, Q., Jaegle, L., Jaffe, D. A., Weiss-Penzias, P., Heckman, A., and Snow, J. A.: Long-range transport of Asian pollution to the northeast Pacific: Seasonal variations and transport pathways of carbon monoxide, J. Geophys. Res.-Atmos., 109, D23S07, doi:10.1029/2003JD004402, 2004.

Lin, M., Holloway, T., Oki, T., Streets, D. G., and Richter, A.: Multi-scale model analysis of boundary layer ozone over East Asia, Atmos. Chem. Phys., 9, 3277–3301, 2009, http://www.atmos-chem-phys.net/9/3277/2009/.

Lin, M., Holloway, T., Carmichael, G. R., and Fiore, A. M.: Quantifying pollution inflow and outflow over East Asia through coupling regional and global models, Atmos. Chem. Phys. Discuss., 10, 109–152, 2010, http://www.atmos-chem-phys-discuss.net/10/109/2010/.

Madronich, S.:The Tropospheric Visible Ultra–violet (TUV) model web page: http://www.acd.ucar.edu/TUV, 2002.

Mao, J., Ren, X., Brune, W. H., Olson, J. R., Crawford, J. H., Fried, A., Huey, L. G., Cohen, R. C., Heikes, B., Singh, H. B., Blake, D. R., Sachse, G. W., Diskin, G. S., Hall, S. R., and Shetter, R. E.: Airborne measurement of OH reactivity during INTEX-B, Atmos. Chem. Phys., 9, 163–173, 2009, http://www.atmos-chem-phys.net/9/163/2009/.

McNaughton, C. S., Clarke, A. D., Kapustin, V., Shinozuka, Y., Howell, S. G., Anderson, B. E., Winstead, E., Dibb, J., Scheuer, E., Cohen, R. C., Wooldridge, P., Perring, A., Huey, L. G., Kim, S., Jimenez, J. L., Dunlea, E. J., DeCarlo, P. F., Wennberg, P. O., Crounse, J. D., Weinheimer, A. J., and Flocke, F.: Observations of heterogeneous reactions between Asian pollution and mineral dust over the Eastern North Pacific during INTEX-B, Atmos. Chem. Phys., 9, 8283–8308, 2009, http://www.atmos-chem-phys.net/9/8283/2009/.

Mena-Carrasco, M., Tang, Y., Carmichael, G. R., Chai, T., Thongbongchoo, N., Campbell, J. E., Kulkarni, S., Horowitz, L., Vukovich, J., Avery, M., Brune, W., Dibb, J. E., Emmons, L., Flocke, F., Sachse, G. W., Tan, D., Shetter, R., Talbot, R. W., Streets, D. G., Frost, G., and Blake, D.: Improving regional ozone modeling through systematic evaluation of errors using the aircraft observations during the International Consortium for Atmospheric Research on Transport and Transformation, J. Geophys. Res.-Atmos., 112, D12S19, doi:10.1029/2006JD007762, 2007.

NRC: Global Sources of Local Pollution: An Assessment of Long-Range Transport of Key Air Pollutants to and from the United States, Washington DC, USA, 2009.

Olivier, J. G. J. and Berdowski, J. J. M.: Global emissions sources and sinks, in: The Climate System, edited by: Guicherit, R. and Heij, B. J., A.A. Balkema Publishers/Swets & Zeitlinger Publishers, Lisse, The Netherlands, 33–78, 2001.

Pfister, G. G., Emmons, L. K., Hess, P. G., Lamarque, J. F., Orlando, J. J., Walters, S., Guenther, A., Palmer, P. I., and Lawrence, P. J.: Contribution of isoprene to chemical budgets: A model tracer study with the NCAR CTM MOZART-4, J. Geophys. Res.-Atmos., 113, D02204, doi:02210.01029/02007JD008797, 2008.

Ramanathan, V., Li, F., Ramana, M. V., Praveen, P. S., Kim, D., Corrigan, C. E., Nguyen, H., Stone, E. A., Schauer, J. J., Carmichael, G. R., Adhikary, B., and Yoon, S. C.: Atmospheric brown clouds: Hemispherical and regional variations in long–range transport, absorption, and radiative forcing, J. Geophys. Res.-Atmos., 112, D22S21, doi:10.1029/2006JD008124, 2007.

Reidmiller, D. R., Jaffe, D. A., Chand, D., Strode, S., Swartzendruber, P., Wolfe, G. M., and Thornton, J. A.: Interannual variability of long-range transport as seen at the Mt. Bachelor observatory, Atmos. Chem. Phys., 9, 557–572, 2009, http://www.atmos-chem-phys.net/9/557/2009/.

Seinfeld, J. H., Carmichael, G. R., Arimoto, R., Conant, W. C., Brechtel, F. J., Bates, T. S., Cahill, T. A., Clarke, A. D., Doherty, S. J., Flatau, P. J., Huebert, B. J., Kim, J., Markowicz, K. M., Quinn, P. K., Russell, L. M., Russell, P. B., Shimizu, A., Shinozuka, Y., Song, C. H., Tang, Y. H., Uno, I., Vogelmann, A. M., Weber, R. J., Woo, J. H., and Zhang, X. Y.: ACE-Asia – Regional climatic and atmospheric chemical effects of Asian dust and pollution, B. Am. Meteorol. Soc., 85, 367—380, 2004.

Shinozuka, Y., Clarke, A. D., DeCarlo, P. F., Jimenez, J. L., Dunlea, E. J., Roberts, G. C., Tomlinson, J. M., Collins, D. R., Howell, S. G., Kapustin, V. N., McNaughton, C. S., and Zhou, J.: Aerosol optical properties relevant to regional remote sensing of CCN activity and links to their organic mass fraction: airborne observations over Central Mexico and the US West Coast during MILAGRO/INTEX-B, Atmos. Chem. Phys., 9, 6727–6742, 2009, http://www.atmos-chem-phys.net/9/6727/2009/.

Singh, H. B., Brune, W. H., Crawford, J. H., Flocke, F., and Jacob, D. J.: Chemistry and transport of pollution over the Gulf of Mexico and the Pacific: spring 2006 INTEX-B campaign overview and first results, Atmos. Chem. Phys., 9, 2301–2318, 2009, http://www.atmos-chem-phys.net/9/2301/2009/.

Skamarock, W. C., Klemp, J. B., Dudhia, J., Gill, D. O., Barker, D. M., Wang, W., and Powers, J. G.: A description of the Advanced Research WRF Version 2, NCAR Tech Notes-468+STR, 2005

Streets, D. G., Bond, T. C., Carmichael, G. R., Fernandes, S. D., Fu, Q., He, D., Klimont, Z., Nelson, S. M., Tsai, N. Y., Wang, M. Q., Woo, J. H., and Yarber, K. F.: An inventory of gaseous and primary aerosol emissions in Asia in the year 2000, J. Geophys. Res.-Atmos., 108, 8809, doi:8810.1029/2002JD003093, 2003.

Tang, Y., Carmichael, G. R., Horowitz, L. W., Uno, I., Woo, J.–H., Streets, D. G., Dabdub, D., Kurata, G., Sandu, A., Allan, J., Atlas, E., Flocke, F., Huey, L. G., Jakoubek, R. O., Millet, D. B., Quinn, P. K., Roberts, J. M., Worsnop, D. R., Goldstein, A., Donnelly, S., Schauffler, S., Stroud, V., Johnson, K., Avery, M. A., Singh, H. B., and Apel, E. C.: Multiscale simulations of tropospheric chemistry in the eastern Pacific and on the U.S. West Coast during spring 2002, J. Geophys. Res., 109, D23S11, doi:10.1029/2004JD004513, 2004a.

Tang, Y. H., Carmichael, G. R., Uno, I., Woo, J. H., Kurata, G., Lefer, B., Shetter, R. E., Huang, H., Anderson, B. E., Avery, M. A., Clarke, A. D., and Blake, D. R.: Impacts of aerosols and clouds on photolysis frequencies and photochemistry during TRACE-P: 2. Three-dimensional study using a regional chemical transport model, J. Geophys. Res.-Atmos., 108, 8822, doi:8810.1029/2002JD003100, 2003.

Tang, Y. H., Carmichael, G. R., Kurata, G., Uno, I., Weber, R. J., Song, C. H., Guttikunda, S. K., Woo, J. H., Streets, D. G., Wei, C., Clarke, A. D., Huebert, B., and Anderson, T. L.: Impacts of dust on regional tropospheric chemistry during the ACE-Asia experiment: A model study with observations, J. Geophys. Res.-Atmos., 109, D19S21, doi:10.1029/2003JD003806, 2004b.

Tang, Y. H., Carmichael, G. R., Thongboonchoo, N., Chai, T. F., Horowitz, L. W., Pierce, R. B., Al–Saadi, J. A., Pfister, G., Vukovich, J. M., Avery, M. A., Sachse, G. W., Ryerson, T. B., Holloway, J. S., Atlas, E. L., Flocke, F. M., Weber, R. J., Huey, L. G., Dibb, J. E., Streets, D. G., and Brune, W. H.: Influence of lateral and top boundary conditions on regional air quality prediction: A multiscale study coupling regional and global chemical transport models, J. Geophys. Res.-Atmos., 112, D10S18, doi:10.1029/2006JD007515, 2007.

Turpin, B. J. and Lim, H. J.: Species contributions to $PM_{2.5}$ mass concentrations: Revisiting common assumptions for estimating organic mass, Aerosol Sci. Tech., 35(1), 602–610, 2001.

Uno, I., Satake, S., Carmichael, G. R., Tang, Y. H., Wang, Z. F., Takemura, T., Sugimoto, N., Shimizu, A., Murayama, T., Cahill, T. A., Cliff, S., Uematsu, M., Ohta, S., Quinn, P. K., and Bates, T. S.: Numerical study of Asian dust transport during the

springtime of 2001 simulated with the Chemical Weather Forecasting System (CFORS) model, J. Geophys. Res.-Atmos., 109, D19S24, doi:10.1029/2003JD004222, 2004.

VanCuren, R. A.: Asian aerosols in North America: Extracting the chemical composition and mass concentration of the Asian continental aerosol plume from long-term aerosol records in the western United States, J. Geophys. Res.-Atmos., 108, 4623, doi:4610.1029/2003JD003459, 2003.

van Donkelaar, A., Martin, R. V., Leaitch, W. R., Macdonald, A. M., Walker, T. W., Streets, D. G., Zhang, Q., Dunlea, E. J., Jimenez, J. L., Dibb, J. E., Huey, L. G., Weber, R., and Andreae, M. O.: Analysis of aircraft and satellite measurements from the Intercontinental Chemical Transport Experiment (INTEX-B) to quantify long-range transport of East Asian sulfur to Canada, Atmos. Chem. Phys., 8, 2999–3014, 2008,
http://www.atmos-chem-phys.net/8/2999/2008/.

Volkamer, R., Jimenez, J. L., San Martini, F., Dzepina, K., Zhang, Q., Salcedo, D., Molina, L. T., Worsnop, D. R., and Molina, M. J.: Secondary Organic Aerosol Formation from Anthropogenic Air Pollution: Rapid and Higher than Expected, Geophys. Res. Lett., 33, L17811, doi:17810.11029/12006GL026899, 2006.

Wolfe, G. M., Thornton, J. A., McNeill, V. F., Jaffe, D. A., Reidmiller, D., Chand, D., Smith, J., Swartzendruber, P., Flocke, F., and Zheng, W.: Influence of trans-Pacific pollution transport on acyl peroxy nitrate abundances and speciation at Mount Bachelor Observatory during INTEX-B, Atmos. Chem. Phys., 7, 5309–5325, 2007, http://www.atmos-chem-phys.net/7/5309/2007/.

Yienger, J. J., Galanter, M., Holloway, T. A., Phadnis, M. J., Guttikunda, S. K., Carmichael, G. R., Moxim, W. J., and Levy, H.: The episodic nature of air pollution transport from Asia to North America, J. Geophys. Res.-Atmos., 105, 26931–26945, 2000.

Zhang, L., Jacob, D. J., Boersma, K. F., Jaffe, D. A., Olson, J. R., Bowman, K. W., Worden, J. R., Thompson, A. M., Avery, M. A., Cohen, R. C., Dibb, J. E., Flock, F. M., Fuelberg, H. E., Huey, L. G., McMillan, W. W., Singh, H. B., and Weinheimer, A. J.: Transpacific transport of ozone pollution and the effect of recent Asian emission increases on air quality in North America: an integrated analysis using satellite, aircraft, ozonesonde, and surface observations, Atmos. Chem. Phys., 8, 6117–6136, 2008, http://www.atmos-chem-phys.net/8/6117/2008/.

Zhang, Q., Streets, D. G., Carmichael, G. R., He, K. B., Huo, H., Kannari, A., Klimont, Z., Park, I. S., Reddy, S., Fu, J. S., Chen, D., Duan, L., Lei, Y., Wang, L. T., and Yao, Z. L.: Asian emissions in 2006 for the NASA INTEX-B mission, Atmos. Chem. Phys., 9, 5131–5153, 2009,
http://www.atmos-chem-phys.net/9/5131/2009/.

Zhang, Q., Jimenez, J. L., Canagaratna, M. R., Allan, J. D., Coe, H., Ulbrich, I., Alfarra, M. R., Takami, A., Middlebrook, A. M., Sun, Y. L., Dzepina, K., Dunlea, E., Docherty, K., DeCarlo, P. F., Salcedo, D., Onasch, T., Jayne, J. T., Miyoshi, T., Shimono, A., Hatakeyama, S., Takegawa, N., Kondo, Y., Schneider, J., Drewnick, F., Borrmann, S., Weimer, S., Demerjian, K., Williams, P., Bower, K., Bahreini, R., Cottrell, L., Griffin, R. J., Rautiainen, J., Sun, J. Y., Zhang, Y. M., and Worsnop, D. R.: Ubiquity and dominance of oxygenated species in organic aerosols in anthropogenically-influenced Northern Hemisphere midlatitudes, Geophys. Res. Lett., 34, L13801, doi:13810.11029/12007GL029979, 2007.